SHEARDY, ALEX T., Ph.D. Experimental and Theoretical Optical Properties of Two Emerging Nanoparticles (2020)
Directed by Dr. Jianjun Wei. 93 pp.

As nanoparticles and materials are introduced into commercial applications, new emerging materials continue to be discovered. Many of these new materials have interesting properties that make them well-suited for use in a variety of fields, including electronics, energy production/storage, sensing, and biomedical. However, before these emerging particles can be used, it is critical that the properties of these materials are well-characterized. Two particular nanoparticles, carbon nanodots (CNDs) and copper sulfide nanoparticles (CuS NPs), are of interest, owing to their unique properties. Specifically, CNDs are of interest in biomedical applications due to their small size and strong fluorescence, though the mechanism of this fluorescence remains unknown. CuS is of interest in many optical and electronic applications due to its near-metallic nature and asymmetrical crystal structure. The nature of both nanomaterials is such that purely experimental characterization is insufficient in exploring the properties of interest. Thus, experimental and theoretical studies of both materials have been explored to better elucidate the properties of these materials. Specifically, both particles have been synthesized, characterized, and modeled using density functional theory. For the study of CNDs, the major findings were in regard to how structural modifications and deformations affect the optical properties and these relations were compared to experimental findings. A novel synthesis of CuS NPs was developed and the charge carrier effective mass and density were studied from a theoretical perspective for the first

time. Additionally, photothermal therapy has been explored as a potential application for the CuS NPs.

EXPERIMENTAL AND THEORETICAL OPTICAL PROPERTIES OF TWO EMERGING NANOPARTICLES

by

Alex T. Sheardy

A Dissertation Submitted to
the Faculty of The Graduate School at
The University of North Carolina at Greensboro
in Partial Fulfillment
of the Requirements of the Degree
Doctor of Philosophy

Greensboro
2020

Approved by

_____
Committee Chair

APPROVAL PAGE

This dissertation written by Alex T. Sheardy has been approved by the following committee of the Faculty of The Graduate School at The University of North Carolina at Greensboro.

Committee Chair _____
Jianjun Wei

Committee Members _____
Liam Duffy

_____
Hemali Rathnayake

_____
Joseph Starobin

_____
Date of Acceptance by Committee

_____
Date of Final Oral Examination

ACKNOWLEDGEMENTS

This work is the culmination of many years of work and would not be possible without the help and support of many others, both professionally and personally. To start with, I have worked with three different research advisors through my previous degrees and this doctorate and I would be remiss if I did not thank all of them; Drs. Paul Pantano, Richard Saykally, and Jianjun Wei. Dr. Pantano helped introduce the world of nanoscience, Dr. Saykally helped me learn the fundamentals of science and the importance of theory, and Dr. Wei helped me to put it all together and guide me. Without the influences of all three, I would not be the scientist I am today.

Additionally, I would like to thank my committee members for helping to advise me through this project; Drs. Liam Duffy, Hemali Rathnayake, and Joseph Starobin. Additionally, this work would not be possible without the help of the staff at JSNN, both past and present, that have helped with both instrumentation and computational difficulties; Drs. Steven Crawford, Kristen Dellinger, Albert Hung, Kyle Nowlin, and Kristen Rhinehardt. There are also many labmates and friends that have helped with various aspects of this work; Dr. Taylor Mabe, Dr. Zheng Zeng, Dr. Yiyang Liu, Dr. Wendi Zhang, Dr. Harish Chevva, Durga Arvapalli, Kokougan Allado, Bhawna Bagra, Zuowei Ji, Anitha Jayapalan, Ziyu Yin, Mengxin Liu, Frank Tukur, Klinton Davis, Matthew Hawkins, Ryan Yarborough, and many others.

From a more personal side, I need to thank all of my friends and family for their support throughout the years. My dad helped introduce me to science and he, my mom,

and my sister have all helped me get through the more difficult parts of my life. Words cannot express how much your support has meant to me. The help and support of my friends has also been invaluable. Finally, I would like to thank the numerous doctors and nurses who have helped me to manage my autoimmune condition and allow me to do the work that I enjoy.

TABLE OF CONTENTS

Page

LIST OF TABLES

Page

LIST OF FIGURES

Page

CHAPTER I

INTRODUCTION

To quote the title of a lecture by famed physicist Richard Feynman "There's Plenty of Room at the Bottom", meaning that there is much research to be done on small scale systems.[1] The major field to which this quote is often applied is that of nanoscale systems, or systems with dimensions of less than 100 nm or 10^{-7} m. As technology has advanced, potential and realized applications in a number of different fields have been explored, including electronics, energy production/storage, sensing, and biological/medical usage. While many of these materials have been implemented into useful applications, new materials that have the potential to be employed in multiple fields are constantly being discovered. However, before these materials can utilized, it is imperative that their properties are well-characterized to ensure that the optimal material is being used.

For this work, two different nanoparticles – carbon nanodots (CNDs) and copper sulfide nanoparticles (CuS NPs) – have been studied as emerging nanoparticles with a number of different applications. Each particle will be introduced more thoroughly in the chapters focusing on their specific study (Chapters 2 and 3, respectively), but a brief introduction is necessary for establishing the motivation of this work. CNDs are zero-dimensional carbon particles typically on the order of a few nanometers (Fig. 1.1, left). The main attractive attributes of CNDs are their small size, biocompatibility, and optical

properties. As such, the primary proposed applications of CNDs are biologically oriented, either for bioimaging, drug delivery, or as a therapeutic. However, unlike the small molecules or inorganic nanoparticles that CNDs are aiming to replace, the chemical structures of CNDs remain poorly understood, and numerous particles fall under the name "CNDs", despite having drastically different properties.[2] CuS, or more accurately Cu_xS ($1 < x < 2$), is an interesting emerging material owing to the dependence of the optical and electronic properties on the stoichiometry of the material (Fig. 1.1, right). Specifically, Cu_2S is a semiconducting material with limited optical properties, but as the relative amount of sulfur increases, the number of free charge carriers (holes) also increases. This leads to two useful properties: an increase in charge carrier density results in increased electrical conductivity; and the movement of these electrons can act as a plasmon, giving rise to interesting optical properties. This combination of properties leads to many potential applications: including catalysis, energy harvesting, and biomedical applications.[3] One such biomedical application of interest is a technique called photothermal therapy. In this technique, a near-infrared laser is used to heat nanoparticles with the goal of this heat inducing apoptosis in cancer cells. Unfortunately, the crystal structure of CuS is asymmetrical in space, resulting in poor understanding on the fundamentals of the opto-electronic properties and inhibiting implementation into any application, including photothermal therapy. Since many characterization techniques are often oriented toward bulk properties, particularly for these very small particles, these properties are often misattributed.

For both of the above described materials, there is a lack of understanding on the nature of the opto-electronic properties that is difficult to approach from a purely experimental tactic. In the case of CNDs, synthetic control and/or specimen characterization at a level scientists currently cannot reach would be required to accurately correlate the structure and properties. Likewise, the asymmetrical three-dimensional properties of CuS makes experimental characterization difficult. The above described difficulties make experimental investigation of these materials incomplete, and thus the remaining option is to model these particles using computational methods. Specifically, quantum mechanical (QM) calculations are required to model these materials as many of these interesting properties are dependent on the electronic structure.

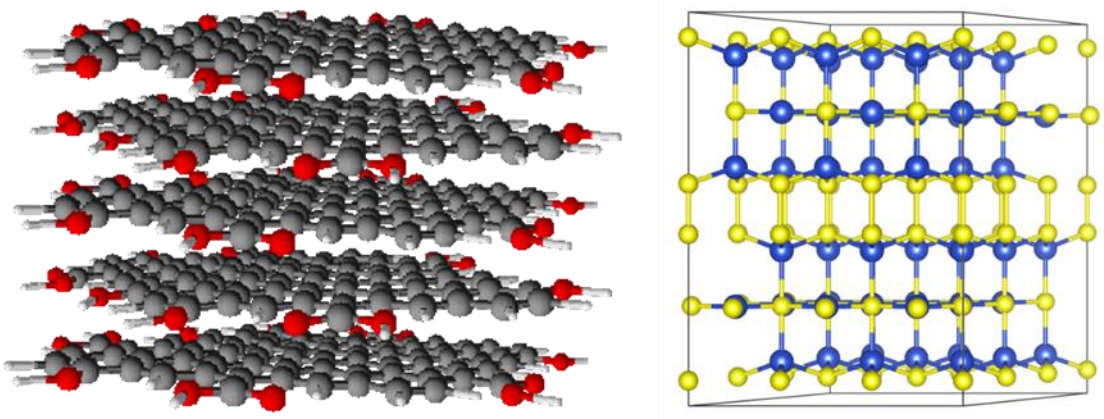

Figure 1.1. Schematic of Studied Structures. A simplified representation of a CND structure (left) and the crystal structure for stoichiometric CuS (right).

The fundamental basis of QM calculations is the time-dependent Schrödinger equation (Eqs. 1.1-2). In this equation, $\hat{T}$ is the kinetic energy term given in Eq. 1.3,

where N is the number of electrons, $\hbar$ is the reduced Planck constant, and m_e is the mass of an electron. The potential energy terms are $\hat{U}$(electron-electron interactions) and $\hat{V}$(electron-nuclei interactions). As directly solving this equation is often quite complicated, the following assumptions are usually made; electron-electron interactions are a relatively small contribution and can be ignored, and the potential is time-independent. This allows the equation to be separated into a time-dependent portion (Eq. 1.4) and a time-independent portion (Eq. 1.5). By solving this equation for a given system, the energy (E_n) and wavefunction (ψ_n) corresponding to state n can be calculated.[4] From these calculations, different steps can be followed in order to extract various useful quantities and/or properties.

$$i\hbar \frac{\delta \Psi(\mathbf{r}, \mathrm{t})}{\delta t} = \hat{H}\Psi(\mathbf{r}, \mathrm{t}) \tag{1.1}$$

$$\hat{H} = \hat{T} + \hat{U} + \hat{V} \tag{1.2}$$

$$\hat{T} = \sum_{i}^{N} \frac{-\hbar^2}{2m_e} \nabla_i^2 \tag{1.3}$$

$$\Psi(\mathbf{r}, \mathrm{t}) = e^{-\frac{iEt}{\hbar}} \psi(\mathbf{r}) \tag{1.4}$$

$$\hat{H}\psi(\boldsymbol{r}) = \left[\hat{T} + \hat{V}\right]\psi(\boldsymbol{r}) = E\psi(\boldsymbol{r}) \tag{1.5}$$

In order to predict the optical properties of a molecular system, the energy difference and transition probability between an initial state (ψ_i) and a final state (ψ_f) are required. Calculation of the energy of a transition is trivial, though typically the wavelength of this transition is of more interest (Eq. 1.6). However, the existence of two

states does not mean that a transition between these states is possible, and the calculation of this probability is somewhat more difficult. While most QM calculations are able to be treated in a time-independent fashion, the interaction of light with a material is fundamentally a time-dependent process, meaning that the potential is now time-dependent. In order to solve this type of problem, a time-dependent perturbation ($\hat{H}'$) is added to the Hamiltonian after solving the system homogeneously (Eq. 1.7). In the case of light, the perturbing potential can be considered as a traveling wave (Eq. 1.8), where *A* is the intensity of the perturbation and ω is the frequency of the light. Solving the first-order perturbation results in the equation referred to as "Fermi's Golden Rule", which gives the probability of a transition from initial state ® to final state f ($\Gamma_{i\to f}$, Eq. 9), where ρ is the density of states around the final state. By combining Eqs. 1.6 and 1.9 the energy and intensity of optical transitions can be found, allowing for prediction of an absorption spectrum.[4]

$$\lambda_{i\to f} = \frac{hc}{E_f - E_i} \tag{1.6}$$

$$\hat{H} = \hat{H}_0 + \hat{H}' \tag{1.7}$$

$$\hat{H}' = Ae^{i\omega t} \tag{1.8}$$

$$\Gamma_{i\to f} = \frac{2\pi}{\hbar}\left|\langle\psi_f|H_0|\psi_i\rangle\right|^2\rho \tag{1.9}$$

The determination of optical properties for non-molecular systems, such as solids, requires a different treatment as increasing the number of atoms results in a loss of discrete energy states and the formation of bands of states. These band structures are the

result of using an infinite periodic potential and determine both the optical and electronic properties of a material. In the case that the highest energy occupied band (valence band) is only partially occupied by electrons, then the material is metallic. Conversely, if the valence band is full, the energetic difference (band gap) between the valence and next highest band (conduction) determines if the material is semiconducting (small band gap) or insulating (large band gap). In the case of semi-conductors and insulators, the optical properties are dependent on the size of the bandgap, as in Eq. 1.6. In the case of metals, the electrons are able to oscillate collectively and the energy of this oscillation occurs at a specific frequency that depends on the size and nature of the material.[5] This phenomenon is referred to as a plasmon and will be discussed more in depth in the context of copper sulfide in Chapter 3.

While these equations can be solved analytically for simple systems, such as particle in a box, harmonic oscillators, and the hydrogen atom, these systems are not accurate representations of most real systems. In the case of even a simple molecule like water, the location and interaction of 11 different bodies (3 nuclei, 8 electrons) are required to solve the Schrödinger equation. As a result, it is not possible to solve this system exactly, and is even difficult to solve numerically without the use of further approximations. Density functional theory (DFT) is a common approximation method for QM calculations on non-trivial systems. Modern DFT is performed using the Kohn-Sham (KS) equations given in Eqs. 1.10 and 1.11.[6-7] The symbols ϕ and ε denote the KS wavefunction and energy, respectively. In typical QM calculations on multi-atom systems the Born-Oppenheimer approximation is used, essentially stating that the nuclei

do not move relative to the electrons. This simplifies the Schrödinger equation to Eq. 1.10 where an effective potential ($v_{eff}(\boldsymbol{r})$, Eq. 1.11) is used. In this effective potential, the nucleus and core-level electrons for a given atom are combined into a single pseudopotential and the pseudopotentials for all atoms are added to give a total effective nuclear potential, $v_{nuc}(\boldsymbol{r})$. The second and third terms in the effective potential are both dependent on electron density, $\rho(\mathbf{r})$, hence the name *Density Functional* Theory. Specifically, the second term corresponds to Coulomb interactions within the electron cloud, while E_{xc} is the so called "exchange-correlation" energy. E_{xc} is essentially defined to make the approximation exactly equal to a real system and is one of the main parameters calculated in DFT calculations.

$$\left(\frac{1}{2}\nabla^2 + v_{eff}(\boldsymbol{r})\right)\phi_j(\boldsymbol{r}) = \epsilon_j\phi_j(\boldsymbol{r}) \tag{1.10}$$

$$v_{eff}(\boldsymbol{r}) = v_{nuc}(\boldsymbol{r}) + \int d^3\boldsymbol{r}'\,\frac{\rho(\boldsymbol{r}')}{|\boldsymbol{r}-\boldsymbol{r}'|} + \frac{\delta E_{xc}}{\delta\rho(\boldsymbol{r})} \tag{1.11}$$

The general methodology for DFT calculations is given in Fig. 1.2. In the first step, the calculation begins by an initial guess of the electron density in the system. This guess is then used to find the effective potential (Eq. 1.11), resulting in full knowledge of the Hamiltonian. Once the Hamiltonian is calculated, the ground state energy and wavefunction can be further calculated. From the wavefunction, a new electron density can be calculated and compared to the initial guess. If the new density matches the previous density the computed Hamiltonian is correct, and all excited states are calculated. Else, the new density is used to calculate a new effective potential and

Hamiltonian. This process is repeated iteratively until the difference between two steps is sufficiently small. Since the aim of this iteration is to reduce the difference between individual steps, this is referred to as a self-consistent field (SCF) calculation. As this process ultimately ends with the calculation of the Hamiltonian for the system and the ground state wavefunction, it is then possible to calculate the energies and wavefunctions for all eigenstates. This method results in a computationally-effective calculation of the electronic properties and allows for predictions to support experiments.

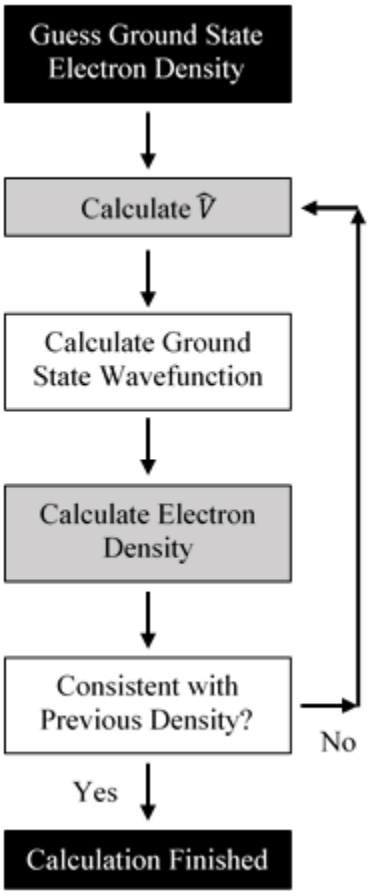

Figure 1.2. General DFT Pathway. Flow-chart showing the general method of the self-consistent calculations used for density function theory.

While this chart represents the general path used for DFT, the way these calculations are performed is dependent on the material and property of choice. DFT is a technique that inherently uses periodic boundary conditions. For crystalline materials, this means that the atoms can be placed both within and on the boundaries of the defined unit cell. The periodic boundaries then result in effectively modeling a bulk material. When performing the integration of Eq. 1.11 the point(s) in reciprocal space, termed *k-points*, over which the integration is performed are an important factor. For crystals, the pathway in Fig. 1.2 is performed using a uniform grid of k-points, referred to as a Monkhorst-Pack grid. For molecules, there are changes made both to the design of the structure for input and the k-points. To make sure that the molecule is effectively isolated from mirror images in periodic boundaries, the atoms are placed in a box much larger than the molecule. Specifically, at least 1 nm between the molecule and its mirror images allows for sufficient isolation. Then, only a single k-point at Γ (0 0 0) is used for the integration.

The above description and accompanying figure (Fig. 1.2) typically only represent the first stage of calculations that can be performed within the DFT framework. A common next step for all systems is a structural relaxation wherein the atoms are slightly moved and another SCF cycle is run, to determine if the energy of the system increases or decreases. As with the SCF process, this step is iterated until the energy difference between consecutive structures is sufficiently small, thus providing the expected physical structure of the target system. Once the structure has been optimized, the subsequent

steps will depend both on the property of interest, but also on the implementation of DFT, a choice that will be discussed next.

As DFT is a fairly common technique for QM calculations there are a number of software packages that have been created to perform these calculations. Generally speaking, there are two types of DFT packages; licensed software and open-source software. The licensed programs are generally well-accepted, include multiple functionalities, and are user-friendly, however the license is often quite expensive. Fortunately, there are several open-source implementations that are equally accurate and functional, albeit at the expense of some user-friendliness. For the work described herein, two different open-source DFT packages were used: Quantum ESPRESSO (QE)[8] and ABINIT.[9] In exploring these two packages, QE is generally a more user-friendly package, which is why it was chosen for the more common types of calculations used for CuS. However, QE's implementation of time-dependent density functional theory (TDDFT) needed for Fermi's Golden Rule calculations (Eq. 1.9) does not give the same level of information that ABINIT gives.[10-11] Essentially, QE simply gives the final product, while ABINIT gives more information about individual transitions. This is the reason that ABINIT was chosen for use in studying CNDs, where these calculations become important.

To use DFT in modeling the optical properties of CNDs and CuS, two different approaches were used. Both models began with the same steps of structural relaxation and the determination of the Hamiltonian as described in Fig 1.2. For CNDs, these steps were performed for a range of different structures, as the exact structure of the material is

unknown. TDDFT calculations were then performed on all the chosen CND structures to generate predicted absorptive transitions. To generate spectra that are representative of realistic experimental data, a Gaussian broadening was performed on the predicted transitions. These results were then analyzed to find correlations between the structures and resulting optical properties. For CuS only a single structure was needed, as the crystal structure of the material is well defined. Following the structural relaxation, band structure and electronic density of states calculations were performed, as these are the governing factors on the optical and plasmonic properties of CuS. For both of the studied materials, experimental syntheses and characterizations were also performed to validate the theoretical results, including a novel synthesis of CuS nanoparticles. The specifics of these calculations and syntheses for CNDs and CuS are given in Chapters 2 and 3, respectively. Photothermal therapy, a potential application that is based on the optical properties of CuS, is introduced and explored in Chapter 4. Taken together, a better understanding on the properties of these materials has been obtained, providing a step closer toward use of these materials in applications, including photothermal therapy.

References

1. Feynman, R. P., There's Plenty of Room at the Bottom. *Caltech Engineering and Science* **1960,** *23* (5), 22-36.

2. Li, H.; Kang, Z.; Liu, Y.; Lee, S.-T., Carbon nanodots: synthesis, properties and applications. *Journal of Materials Chemistry* **2012,** *22* (46), 24230-24253.

3. Liu, Y.; Liu, M.; Swihart, M. T., Plasmonic Copper Sulfide-Based Materials: A Brief Introduction to Their Synthesis, Doping, Alloying, and Applications. *The Journal of Physical Chemistry C* **2017,** *121* (25), 13435-13447.

4. Griffiths, D. J.; Schroeter, D. F., *Introduction to Quantum Mechanics, 3rd Edition*. Cambridge University Press: Cambridge, 2018.

5. Kittel, C., *Introduction to Solid State Physics, 8th Edition*. Wiley: 2004.

6. Jones, R. O., Density functional theory: Its origins, rise to prominence, and future. *Reviews of Modern Physics* **2015,** *87* (3), 897-923.

7. Kohn, W.; Sham, L. J., Self-Consistent Equations Including Exchange and Correlation Effects. *Physical Review* **1965,** *140* (4A), A1133-A1138.

8. Giannozzi, P.; Baroni, S.; Bonini, N.; Calandra, M.; Car, R.; Cavazzoni, C.; Ceresoli, D.; Chiarotti, G. L.; Cococcioni, M.; Dabo, I.; Dal Corso, A.; de Gironcoli, S.; Fabris, S.; Fratesi, G.; Gebauer, R.; Gerstmann, U.; Gougoussis, C.; Kokalj, A.; Lazzeri, M.; Martin-Samos, L.; Marzari, N.; Mauri, F.; Mazzarello, R.; Paolini, S.; Pasquarello, A.; Paulatto, L.; Sbraccia, C.; Scandolo, S.; Sclauzero, G.; Seitsonen, A. P.; Smogunov, A.; Umari, P.; Wentzcovitch, R. M., QUANTUM ESPRESSO: a modular and open-source software project for quantum simulations of materials. *J Phys Condens Matter* **2009,** *21* (39), 395502.

9. Gonze, X., A brief introduction to the ABINIT software package. In *Zeitschrift für Kristallographie - Crystalline Materials*, 2005; Vol. 220, p 558.

10. Casida, M. E., Time-Dependent Density Functional Response Theory for Molecules. 1995; Vol. 1, pp 155-192.

11. Casida, M. E.; Jamorski, C.; Casida, K. C.; Salahub, D. R., Molecular excitation energies to high-lying bound states from time-dependent density-functional response theory: Characterization and correction of the time-

dependent local density approximation ionization threshold. *The Journal of Chemical Physics* **1998,** *108* (11), 4439-4449.

CHAPTER II

EXPERIMENTAL AND TIME-DEPENDENT DENSITY FUNCTIONAL THEORY MODELING STUDIES ON THE OPTICAL PROPERTIES OF CARBON NANODOTS

Introduction

First discovered by accident in 2004 by Xu *et al*.,[1] carbon dots (CDs) have been a focus of research for a wide variety of applications, including bioimaging and theranostics,[2-6] drug delivery,[7-9] antioxidation,[10-13] and use in solar cells.[14-15] Depending on the desired application, a wide variety of synthetic approaches can be used, and these varied methods result in varied structures and properties.[16-18] This is because, unlike traditional metallic and inorganic semiconducting nanoparticles which possess well-defined crystalline structures, the true structure of CDs is non-obvious. In fact, using the language of Zhu *et al*.,[19] "carbon dots" can be further divided into three subgroups; graphene quantum dots (GQDs), carbon nanodots (CNDs), and polymer dots (PDs). These particles are listed in order of increasing sp^3 character, with GQDs being almost entirely graphitic, CNDs possessing a mixture of graphitic and diamond-like character, and PDs contain small sp^2 domains linked by larger polymer (sp^3) chains. The mixture of

graphitic and diamond-like structures in CNDs leads to their unique optical properties, but also makes prediction of these properties an interesting challenge.

The major defining differences between synthetic methods are the carbon sources being used to produce the CNDs. Generally, there are two routes that can be used to produce CNDs; top-down and bottom-up approaches. Top-down methods start with large carbonaceous materials (graphite, carbon nanotubes, etc.) which are then broken down into smaller particles. Since the source materials start with graphitic structures, the produced CNDs maintain this hybridization, but often need post-synthetic modification and/or doping to achieve photoluminescence (PL).[19-21] Bottom-up methods start with smaller molecules such as carbohydrates,[3, 5, 15] alcohols,[22] and citric acid,[23-26] among others,[7, 27-28] which are reacted to form larger particles. The increased variety of starting materials results in highly diverse structures and compositions. In addition to carbon, most CNDs contain oxygen, while others may also incorporate nitrogen,[23, 29] sulfur,[12, 30-31] and/or phosphorous.[32] The different structures and compositions can lead to different properties and potential applications.

One of the main advantages of CNDs over other materials is that the synthesis can often be performed in a way that allows for ideal properties for a given application. For example, our group has shown that both carboxylic acids and amines can contribute to the anti-oxidative properties of CNDs,[10] and these properties can be further enhanced by the addition of sulfur.[12] CNDs can also exhibit excitation-dependent fluorescence, which can be helpful for bioimaging or solar conversion applications.[15, 19, 29] Alternatively, some groups have synthesized CDs that do not show excitation-dependent fluorescence.[5,

[30] The specific energy and quantum yield is dependent on the surface functionality,[19] though reports are often conflicting on the exact way the functionality affects the photophysics.

The complicated and diverse nature of CND structures makes an empirical synthetic study on the nature of the optical properties of CNDs a futile effort. For example, simply changing a single precursor molecule to change the functional groups may also result in changes to the structure in ways that cannot be predicted. The addition of the functional group may result in changes to either the surface functionality and/or the graphitic structure, both of which can change the optical properties. There have been some attempts to study the optical properties of CNDs computationally, but these efforts have been focused on the specific particles synthesized in those works. Specifically, Strauss *et al.* studied the optical absorption/emission properties of six possible CND structures with density functional theory (DFT); and all of the studied structures contain both oxygen and nitrogen atoms.[26] Similarly, the graphene quantum dots studied with DFT by Jin *et al*. contain nitrogen, but no oxygen.[33] Li *et al*. used DFT to explore the structure of some oxygen- and/or sulfur-doped CNDs, but did not study the optical properties of these particles.[31] As such, there remains a lack of understanding on the relationship between the structure and optical properties of CNDs. Herein, we present two example syntheses to showcase the different optical and structural properties that can be observed in CNDs. Further, we used time-dependent DFT (TDDFT) to predict the optical absorption of twelve possible CNDs structures and attempt to correlate the observed optical properties with the structure of the particles.

Experimental

Synthesis of CNDs

Two different syntheses were used to produce carbon nanodots with different properties. The first synthesis was based on the procedure of Hu *et al.*[23] Specifically, this synthesis involved combining 960 mg citric acid (ACROS Organics) and 1 mL ethylene diamine (Fisher Scientific) in 1 mL DI H_2O. This mixture was then heated in a microwave synthesizer (CEM Discover) at 300 W for 18 minutes. The resulting solid was then dissolved in 5 mL DI H_2O, resulting in a dark red-brown solution. Throughout the rest of the text, these particles will be referred to as E-CNDs. Alternative, a variation of the synthesis by Bhunia *et al.*[3] was used. In this procedure, 1.5 g sucrose (Sigma-Aldrich) was first dissolved in 5 mL DI H_2O, and the solution was placed in an ice bath. To this solution, 5 mL conc. hydrochloric acid (12.1 M, Acros Organics) was slowly added (dropwise) to minimize heating. The mixture was heated at 90 °C for 25 minutes, and then cooled and placed in an ice bath. To neutralize the HCl, ~3.2 mL NaOH (18.94 M, Fisher Scientific) was slowly added, again minimizing heating. These particles will be referred to as suc-CNDs throughout the remainder of the text. Following either synthesis, the particles were purified by dialysis (1000 MWCO) and dried by freeze drying to obtain solid products.

Characterization of CNDs

A number of different characterization techniques were used to determine the structure and properties of the synthesized CNDs. The size of the particles was determined using atomic force microscopy (AFM), since the small size and low contrast

makes TEM difficult to obtain. For the AFM, a solution of the particles was drop cast onto a freshly-cleaved mica surface. Due to equipment failure, the suc-CNDs were measured on an Agilent 5600LS AFM, while the E-CNDs were measured with an Asylum MFP-3D Origin+ AFM, but each image was acquired using similar parameters and probes. UV-Vis (Varian Cary 6000i) and fluorescence (Horiba Fluoromax-4) spectroscopies were used to measure the optical properties of the materials. FT-IR, ^{1}H NMR, and ^{13}C NMR (Agilent) were performed on the CNDs to determine the functional groups present on these materials. NMR spectra were obtained by dissolving the samples in D_2O and are averaged over 32 (^{1}H) or 10000 (^{13}C) scans. XPS (Thermo Escalab Xi+) was performed to analyze the elemental composition of each sample. XRD (Agilent) and Raman (Horiba Raman Confocal Microscope) were performed to provide insight into the structure of both particles.

DFT Modeling of CNDs

To model the optical properties of different CND structures, time-dependent density function theory (TDDFT) calculations were carried out on multiple structures using ABINIT.[34-38] The structures start with a pure graphitic sheet ($C_{70}H_{22}$), to which different functionalities including hydroxides, carboxylic acids, epoxides and amines were added, but on the exterior of the sheet and as internal defects. To treat each molecule as isolated, the structures were placed in a 60 × 60 × 25 Bohr box. The calculations were performed by first relaxing structures using a tolerance on the difference of force of 5×10^{-6} Hartree/Bohr, with a maximal force of 5×10^{-5} Hartree/Bohr. Following this is an additional energy relaxation with energy difference cutoff of 1×10^{-7}

Hartree. Finally, the TDDFT calculation is performed using a tolerance on wavefunction squared residual of 10^{-9}. For the TDDFT to be performed, only a single k-point at Γ (0, 0, 0) can be used. These experiments result in relaxed structures of the molecules, the energy eigenstates, and the transition probabilities between eigenstates.

Results and Discussion

CNDS were successfully synthesized using the above described methods. UV-Vis and PL emission spectroscopies were performed for both samples (**Figure** 2.1). In the UV-Vis spectrum, both samples exhibit high intensity absorption around 220 nm which gradually decreases at higher wavelengths. However, the shape of these decreases is noticeably different between the two different synthetic methods. After the strong peak at 200 nm, the E-CNDs have a small shoulder around 230 nm, then the absorbance rapidly drops until there is a strong peak at 350 nm. For these particles, no significant absorbance is observed above ~400 nm. The suc-CNDS on the other hand have a much slower decrease, with two shoulders at 285 and 350 nm and continue to have a decaying absorbance up to ~600 nm. For the PL studies, the E-CNDs exhibited a strong signal at 450 nm, while the suc-CNDs had a much weaker emission at 445 nm.

AFM was performed to determine the size of the particles, specifically by using the height of the particles since the resolution in the XY plane is limited by the AFM probe (**Figure** 2.1C-D). From the AFM height profiles (**Figure** 2.1E-F), both synthetic methods result in sizes on the order of 1.5 - 3 nm. The average sizes for the particles are 1.4 and 2.1 nm for the suc-CNDs and E-CNDs, respectively, and size distributions can be found in Fig. A.S1. FTIR spectroscopy was performed on each type of CND, which

reveals the presence of different functional groups (Fig. A.S2). Specifically, both structures have O-H and C-H stretches at 3300 and 2920 cm^{-1}, respectively. However, the area around the O-H stretch on the E-CNDs possesses additional features, likely from N-H stretches. Additionally, while each spectrum presents peaks at ~1635 cm^{-1} for C=O stretches, this peak is significantly more intense in the E-CNDs. The E-CNDs also feature a prominent peak at 1535 cm^{-1}, which can be attributed to the N-H bend. Both structures have peaks in the 1300-1400 cm^{-1} region arising from C=C stretches. Finally, the suc-CNDs have a medium strength peak at 1025 cm^{-1} which can arise from the C-O stretching.

Both ^{1}H and ^{13}C NMR were performed on the two samples to further analyze the potential functional groups (Fig. A.S3). The complex nature of CND structure makes exact interpretation of the NMR difficult, but specific functional groups can be identified based on peak shifts. For both samples and both ^{1}H and ^{13}C NMR there are clearly aliphatic and hydroxyl hydrogens/carbons. Additionally, there are ^{13}C peaks in the 150-180 ppm region, indicating C=O and/or C=C. However, only the suc-CNDs have a strong ^{1}H signal in this region, indicating that the C=O can only be either a carboxylic acid or ketone, and that the outside of the graphitic structure is likely functionalized with heteroatoms (i.e., OH groups). The ^{1}H signal at 8.3 ppm is likely due to aromatic hydrogens, so the surface of these CNDs is not entirely functionalized. While no carboxylic acid hydrogens are observed, this may easily be attributed to proton/deuterium exchange with the solvent (D_2O). Finally, the ^{1}H NMR for the E-CNDs shows a peak at ~2.8 ppm and several at 5.8 ppm, which can be correlated to amines and amides,

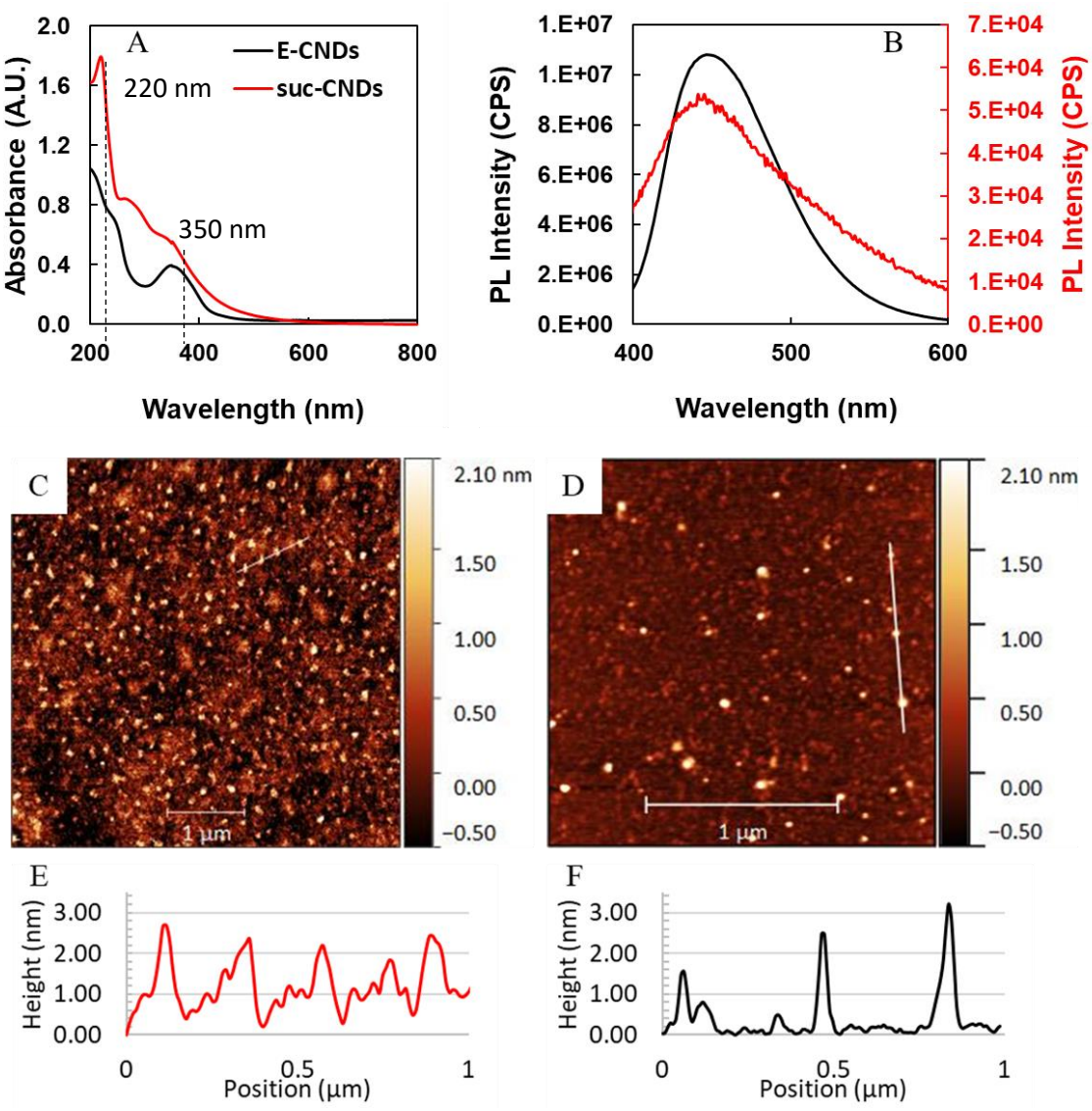

Figure 2.1. UV-Vis, PL, and AFM of CNDs. UV-Vis (A) and PL (B) spectroscopies of both E-CNDs (black) and suc-CNDs (red). The PL data needed to be plotted on separate y-axes due to large differences in the magnitude of the PL signal. For the UV-Vis, both samples were at a concentration of 0.1 mg/mL, while for the PL measurements the concentrations were 0.05 mg/mL. AFM of suc-CNDs (C), E-CNDs (D), and associated height profiles along the lines shown on the AFM image (E, F, respectively). The scale bar on each AFM image is 1 µm.

respectively. Summarizing the results of both FTIR and NMR; both structures have characteristics of graphitic cores covered with oxygenaceous functional groups (hydroxyls, carboxylic acids), while the E-CNDs also have nitrogenous groups (amines and amides).

In order to determine the elemental composition of each sample, XPS was performed (Fig. A.S4A). The suc-CNDs were found to contain 62% carbon and 38% oxygen, while the E-CNDs contained 57% carbon, 22% nitrogen and 20% oxygen. To determine if the CNDs possess a graphitic or amorphous structure, XRD (Fig. A.S4B) and Raman (Fig. A.S4C) were also performed. Both CNDs present broad peaks corresponding to the (002) index,[39] however these peaks do occur at different angles. Specifically, the suc-CND peak is centered at ~17.8° (FWHM = 13°), corresponding to a lattice spacing of 0.47 Å, while the E-CND peak is centered at 23.2° (FWHM = 12.6°) corresponding to a lattice spacing of 0.39 Å. Finally, in the Raman spectra for these samples both D and G peaks can be seen, with D/G ratios of 1.15 and 1.29 for suc-CND and E-CNDs, respectively. The broadness of both the XRD and Raman peaks indicates that the particles are amorphous, however the presence of the (002) peak shows there is a graphitic character to both of these particles.[11, 16, 40] Further, the different angles for the (002) peak suggest that the functionalization of the graphitic structure is different between the particles. Specifically, the larger lattice spacing of the suc-CNDs, combined with the higher oxygen content suggests a larger degree of internal oxygen functionalization on the graphitic structure compared to the E-CNDs. However, the smaller D/G ratio for the suc-CNDs shows that there may be larger amorphous regions

within the structure of the E-CNDs. One possible explanation for these combined results is that the suc-CNDs include a structure resembling layers of graphene oxide within amorphous bulk, while the E-CNDs have less oxidized graphitic regions surrounded by amorphous/polymeric regions. Additionally, the size of the graphitic lattice is expected to largely determine the wavelength of the fluorescence emission, [41-42] and since both particles have similar emission wavelengths, similarly sized graphitic structures are expected for both CNDs.

The differences between these particles, particularly in regard to the PL emission intensity and the strong absorption peak at 350 nm, led to the question: what is responsible for these differences? At quick inspection, the most obvious differences between these syntheses are the presence of nitrogenous functional groups in the E-CNDs, and the increased degree of internal graphitic functionalization in the suc-CNDs. While a comprehensive synthetic study using varying elemental compositions would be possible, the complex structural nature of CNDs makes this approach incomplete. Instead, it is far more reasonable to compare theoretical spectra from a number of different potential CND structures (**I-XII** in Fig. A.S5). The first structure calculated was a simple graphitic sheet (**I**) with no functional groups. This structure is likely not very representative of the materials synthesized but does provide a baseline for looking at the effects of functional groups on the absorptive properties. All other structures were based on this sheet, starting with the addition of both hydroxides and carboxylic acids (**II**), which are present on all following structures. From here, multiple internal defects/functional groups were added, including a 5-7-7-5 Stone-Wales defect (**III**),

hydroxides (**IV**), epoxides (**V**) and a combination of hydroxides and an epoxide (**VI**). The remaining structures started to incorporate nitrogen both as surface and internal functional groups. Specifically, first only external primary amines were added (**VII**), followed by those groups with internal secondary amines disrupting the graphitic lattice (**VIII**), and a combination of structures **VI** and **VIII** having internal oxygens and nitrogens (**IX**). Finally, a series of structures containing 2, 4, or 6 internal tertiary amines were studied (**X**, **XI**, and **XII**, respectively). All structures have an approximate length of 1.2 nm along both the zigzag and armchair sides prior to relaxation, which is on the lower end of the size scale for CNDs. However, increasing the number of atoms greatly increases the computational time and resources required for these calculations. This is also the reason that only a single sheet was modeled for each structure. While the studied structures do not represent the complete amorphous structure of the CNDs, the sp^2 regions largely determine the optical properties of these materials[41-42] and this sized graphitic region is expected to approximate the observed experimental fluorescence.[33, 43]

Using DFT, optimized geometries for each of the above structures were generated (Figure 2.2). As could be expected, structures with only external functional groups (**I**-**II**, **VII**) and structures that have tertiary nitrogens within the graphitic lattice (**X**-**XII**) are still fairly planar. However, the remaining structures with disruptive internal functional groups do show significant deviations for a planar graphene sheet. To analyze these disruptions, the positions of the carbon atoms in the relaxed structures was extracted and fit to a plane using MatLab and the root mean square (RMS) error of this fit is an estimate of planarity (Table 2.1, Fig. A.S6). This value will be used in the spectral analysis.

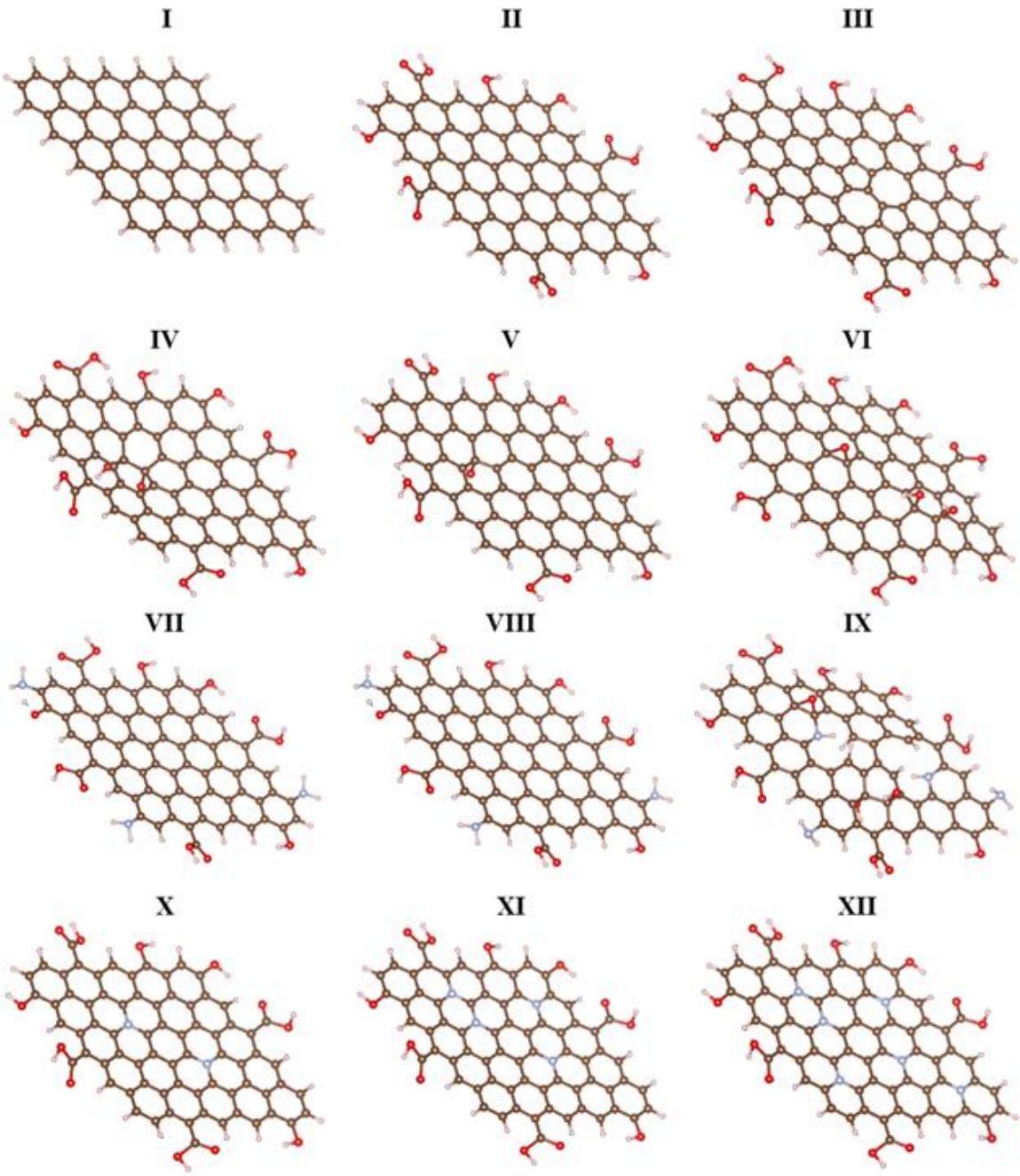

Figure 2.2. DFT-Optimized Structural Geometries. DFT-optimized geometries for structures **I-XII**. Dark gray atoms are carbon, light gray are hydrogen, red are oxygen, and blue are nitrogen.

Table 2.1. Summary of CND Calculated Results. Summary of results from calculations for structures **I-XII**. Included are the root mean square (RMS) error of the fitting of carbon atoms to a plane, height of the π-π* transition, the number of allowed and possible transitions, and the percent of allowed transitions.

Structure	RMS	Peak Height	Allowed Transitions	Possible Transitions	% Allowed Transitions
I	0.006	7.599	364	1812	20.1%
II	0.079	6.112	1370	2730	50.2%
III	0.129	5.323	1442	2730	52.8%
IV	0.257	4.498	1795	2828	63.5%
V	0.154	4.941	1605	2772	57.9%
VI	0.298	4.288	2042	3075	66.4%
VII	0.072	5.894	1576	3060	51.5%
VIII	0.279	4.630	1910	3015	63.3%
IX	0.341	3.604	2332	3376	69.1%
X	0.073	4.997	1501	2772	54.1%
XI	0.071	3.793	1741	2758	63.1%
XII	0.067	5.571	1450	2744	52.8%

Following the structural relaxation, TDDFT calculations were performed to examine the electronic spectra of the tested structures. These calculations result in the energies and probabilities for the transitions from the occupied to unoccupied states. Further analysis of the results was also performed using several different approaches. First, to generate realistic looking electronic spectra, each of the transitions was broadened into a gaussian function with a FWHM of 2.5 nm and all the gaussian functions were added together (Figure 2.3A). A representative final spectrum and stick spectrum showing the original data is found in Figure 2.3B, and the remaining spectra can be found in Fig. A.S7. Second, the number of allowed transitions (oscillator strength $> 10^{-6}$) was compared to number of possible transitions to get a percentage of allowed transitions. Finally, the summed intensity of the major π-π* transitions and the percent of

allowed transitions were compared against the root mean square (RMS) error of the planar fitting (Figure 2.3C). The data from these results in summarized in Table 2.1.

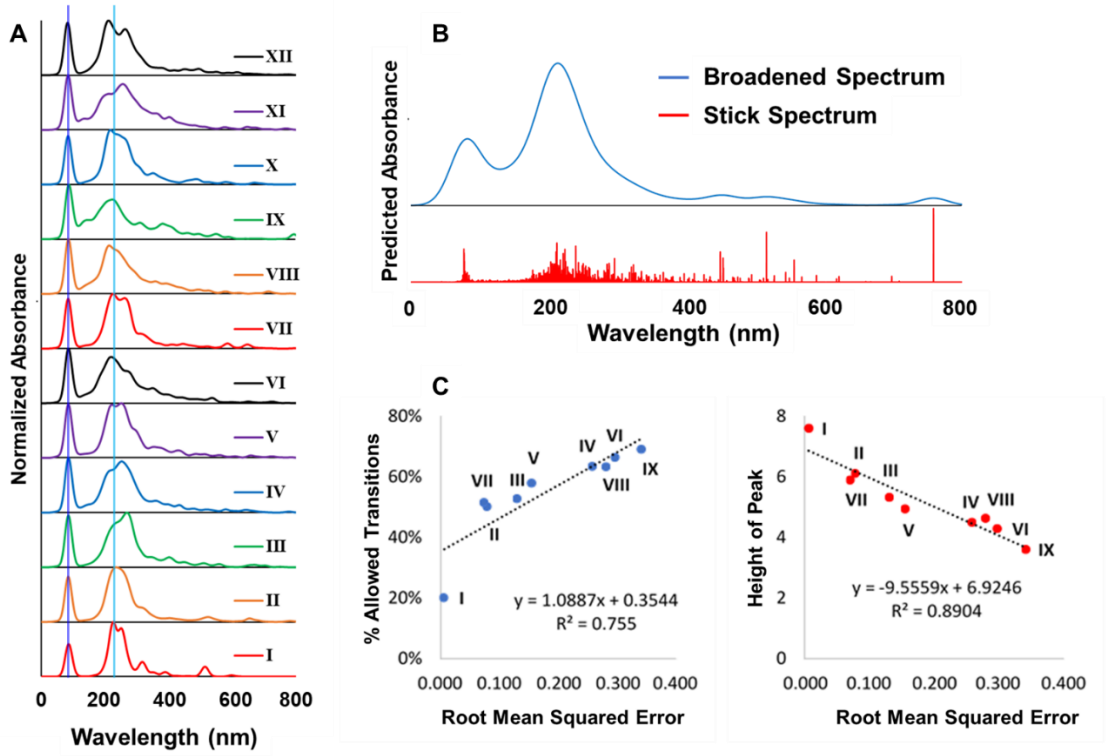

Figure 2.3. Predicted UV-Vis Absorption of CNDs and Observed Trends. (A) Predicted UV-Vis absorption spectra for structures **I-XII**. These spectra have been normalized to the most intense peak and offset for clarity. (B) Representative gaussian broadened (blue) and stick (red) spectra from structure **II**. (C) Plots of the percent of allowed transitions (left, blue dots) and the height of the π-π* transition (right, red dots) vs. the root mean squared error of the fitting of the optimized structure to a plane. The dotted line represents a linear fit of the data, and the equation and R^2 of the fit are given.

Looking at the produced spectra, there are clearly two major peaks/sets of peaks at ~90 nm and between 150-400 nm present for all molecules. For clarity, the presented spectra have been normalized by the intensity of the strongest peak, but any following arguments referring to peak intensity are based on the unnormalized data. From the data,

the peak at 90 nm is a σ-π* transition and does not seem to vary significantly in terms of position, width, or intensity between the different structures. Additionally, this peak is at too high energy to be detected by a standard UV-Vis spectrometer and is therefore not present in the experimental spectra. The peak(s) around 150-400 nm result from π-π* transitions and do vary greatly in position, width, intensity, and number. Representative wavefunctions showing these transitions in structure **II** can be found in Figure 2.4. Before discussing specifics relating to functional groups, some of the observed bulk trends shall be discussed. For structures **I**-**IX** (**X**-**XII** do not follow these trends and will be discussed later) two general trends were observed regarding the planarity of the molecule (RMS error) and the number of allowed transitions or the intensity of the π-π* transition. Specifically, the number of allowed transitions increases roughly linearly (R^2=0.76) with the RMS error, through this trend shows even higher linearity (R^2=0.97) if the pure graphitic structure (**I**) is not included. Conversely, the intensity of the π-π* transition decreases linearly (R^2=0.89) with increasing RMS error.

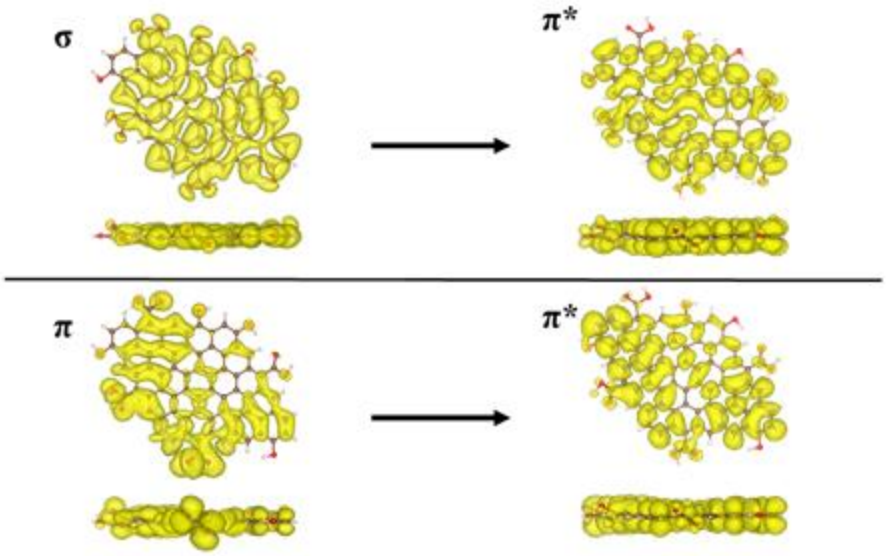

Figure 2.4. Wavefunctions for DFT Transitions. Representative σ-π* transition (top) and π-π* transition (bottom) for structure **II**. The yellow represents the wavefunction.

Taken together, the above-mentioned trends suggest the following behavior; as structural distortions increase, the strength of individual transitions decreases, while new transitions become allowed. For the graphitic structure (**I**) the ideal planar structure results only in transitions between specific states with a high degree of wavefunction overlap. As new functional groups are added, the structure distorts and the overlap of those wavefunctions decreases. However, these structural distortions also result in overlap between states that previously did not overlap. The newly introduced transitions will also fall at slightly different energies than the previous transitions, introducing more width to the peak. While the introduction of functional groups also adds new types of states, the significant increase in the percent of allowed transitions suggests that this trend is due to the change in the graphitic structure rather than any new functional group-dependent transitions. Further, while the small deviations from linearity are likely due to

the specific functional groups, this data does suggest that the most important factor in determining the optical properties of CNDs is the number of disruptive functional groups, rather than the specific elements present. Finally, the experimental spectra show a peak/shoulder at 350 nm, which is generally attributed to n-π* transitions, but is not observed in the predicted spectra.[44] An explanation for this is that the functional groups leading to the n-π* transition must be resonance-isolated from the main graphitic structure which has too many π* states to result in a single peak.

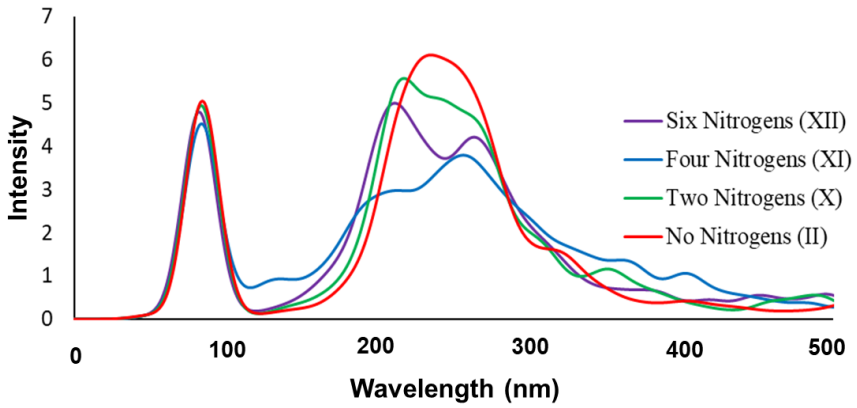

Figure 2.5. Predicted UV-Vis Absorption for N-doped CNDs. Predicted UV-Vis absorption spectra for structures **II** and **X-XII**, structures where carbon atoms in the graphitic structure have been replaced by 0, 2, 4, or 6 nitrogen atoms, respectively.

The major exceptions to this rule are the structures that contain internal tertiary amines (**X-XII**), the spectra for which are shown in Figure 2.5, along with the nitrogen-less analog (**II**). From Table A.S1, there is a slightly decreasing trend in the planarity of these structures, but the spectra show more significant differences than the previous discussion would predict. It can be seen that there is a single major peak around 250 nm in the absence of nitrogen, but as nitrogens are introduced the peak weakens and

separates into multiple peaks/shoulders. Increasing from zero to four nitrogens, the peak consistently lowers in intensity and broadens, however the structure with six nitrogens appears between the two and four nitrogen structures. This suggests that as nitrogen defects in the graphitic lattice are added, the overlap between transitions also improves, potentially due to the lone pair of electrons in the p-orbital of the nitrogen. Further, these trends might help explain the difference in the observed experimental spectra, but more data would be needed to confirm this hypothesis.

The combination of these experimental and computational results, along with an observation by Fu *et al*. might help in explaining the difference in fluorescence intensity between the suc-CNDs and E-CNDs.[45] Specifically, Fu *et al*. observed that the fluorescence intensity increases with decreasing interlayer distance, due to the presence of trap states between graphitic layers. The XRD results for E-CNDs clearly show a decreased interlayer distance of 0.39 Å vs. 0.47 Å for the suc-CNDs. Incorporation of nitrogen atoms within the graphitic lattice does not noticeably disrupt the planarity of the structure, allowing for closely packed layers and higher fluorescence, as seen in the nitrogen containing E-CNDs. Conversely, high oxygen content can cause larger disruptions to the planar structure, resulting in larger interlayer distances and weaker fluorescence, as seen in the suc-CNDs.

As previously stated, certain optical properties (overall height of peak, allowed transitions/width) of CNDs seems to be primarily dominated by the distortions within the graphitic structure, regardless of the specific functional groups. Regarding the shape of the π-π^* transition peak, nearly all of the studied structures show at least two peaks in this

200-300 nm range, the main exception being structure **II**. However, this peak is still asymmetrical, indicating that it may be composed of multiple groups of transitions. While multiple peaks are present for each structure, the relative intensities and positions of each do change with the functional groups present. For example, structures **IV**-**VI** (those containing internal alcohols and/or an epoxide) present similar spectra, with two peaks/shoulders at ~220 and ~250 nm. The introduction of the hydroxide groups in structures **IV** and **VI** leads to similar structural disruptions and overall peak intensity in both samples, and these groups are more disruptive than only having an epoxide. Adding only surface primary amines (**VII**) has little effect on the optical properties, but internal secondary amines (**VIII**-**IX**) do introduce significant distortions and the corresponding spectral changes related to these distortions.

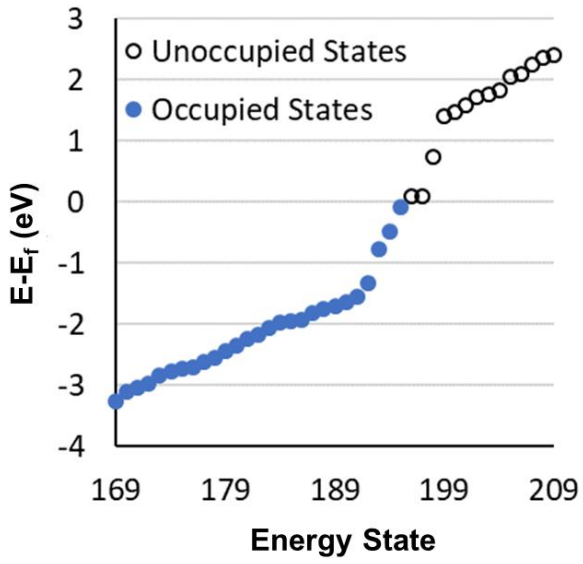

Figure 2.6. Occupied and Unoccupied Electronic States for CNDs. Plot of occupied (blue) and unoccupied (black hollow) states present in structure **II**. The energy on the y-axis is relative to the Fermi energy.

An important factor in discussion is the actual electronic structure of the proposed CND structures, and how this relates to the generated spectra. For this discussion, the available electronic levels and their room temperature occupations for structure **II** are given in Figure 2.6. These energy levels can give information about the energy of fluorescent photons that can be emitted from the structure, but prediction of fluorescence intensity is dependent on factors such as surface passivation and is therefore harder to predict. As can be seen, the major transitions do not come from HOMO-LUMO excitations, as the HOMO-LUMO gap is only 0.16 eV (~7750 nm). Considering that pure infinite graphene is a zero-bandgap semiconductor,[46] it is not surprising that a smaller graphitic sheet has a small bandgap. Using this specific structure as an example, the transitions between 195 occupied and 14 unoccupied states were calculated. These states are numbered according to increasing energy (Figure 2.6), with state 1 being the lowest energy occupied state, state 195 being the HOMO, and state 196 being the LUMO. As previously mentioned, the highest energy transition at 90 nm is a σ-π^* transition, specifically with the transition between states 50 and 205 being a major contributor (Figure 2.4, top). For the π-π^* transitions, a higher energy occupied state is excited to a low-lying unoccupied state, for example the excitation from state 173 to 206 is a significant contribution (Figure 2.4, bottom). This does suggest that π-π^* transitions may be more important than n-π^* transitions in determining the optical properties, at least in terms of excitation. The produced electronic structure may also help to explain the excitation-dependent fluorescence observed in some CNDs[15, 19, 29]. Since there are clearly multiple energy levels that have similar energies, different incident excitation

energies can excite either different energy electrons, or the same electron to a different energy, resulting in different energy PL. Since the majority of the energy levels are either π or π*, this suggests that excitation-independent fluorescence would likely arise from CNDs with smaller aromatic systems, such that there are fewer possible transitions.

Further, while the introduction of new functional groups is expected to change the electronic structure of these particles,[42-43] this cannot be the sole explanation for the observed changes. Specifically, the two factors that have been correlated to planarity; peak intensity and % allowed transitions cannot be explained by changes to the electronic structure alone. For example, the only difference between structures **II** and **IV** is the addition of two hydroxyl groups. Structure **II** has 195 occupied states, while **IV** has 202 occupied states and the same number of unoccupied states (14) was used for both. This is expected, as a single C-C π orbital is removed while 2 C-O σ bonds, 2 O-H σ bonds, and 4 non-bonding oxygen orbitals are added. Therefore, the changes expected purely from the loss and introduction of new electron states is not expected to have a significant effect on the π-π* absorption. However, the observed result is that the peak absorption intensity decreases from 6.1 to 4.5, while the number of allowed transitions increases by 425, even though only 98 new possible transitions are introduced. The removal of a C-C π orbital can cause further changes to the electronic structure, but the significant changes in the transition probability are attributed to structural deformations and increases/decreases in orbital overlap.

In comparing the experimental results to the computation results, it is clear that there are some discrepancies between the two. However, many of these discrepancies

can be explained by one of the fundamental challenges in the study of CNDs: uniformity. While repeated syntheses under identical conditions will yield particles with the same overall properties, the properties of particles from a given synthesis cannot be ascribed to an individual structure. This is the reason that many CNDs exhibit broad peaks in a number of different characterization techniques; for an example Raman, XRD, UV-Vis, and PL. One of the inconsistencies between the theory and the experiment is the presence of theoretical absorption peaks at wavelengths longer than ~500 nm, which are not observed in the experimental results. An explanation for this is simply the energy of these transitions varies from structure to structure, and a real CND sample is likely a combination of these and/or other structures. Averaging the predicted spectra for some combination of the studied structures would result in minimal absorption at longer wavelengths, as shown in the experimental results. To exactly compare experimental and theoretical studies on CNDs, extraordinary purification and characterization techniques would be required to ascertain exact chemical structure and guide theoretical predictions. As such, the aim of this work is not to exactly compare the experimental and theoretical results, but rather to provide some insight into general trends on how functionalization can affect the properties of CNDs.

Conclusion

In conclusion, two CND syntheses with similar size but different optical properties have been presented as a comparison. The major structural difference between the suc-CNDs and the E-CNDs is the presence of nitrogenous functional groups in the E-CNDs. As a result, these particles have orders of magnitude higher PL emission, and a

more distinct absorption peak around 350 nm. To better understand the absorptive optical properties of CNDs, TDDFT was performed on twelve potential CND structures. The predicted absorption results show that the π-π^* transition height is inversely correlated with the disorder of the structure, while the percent of allowed transitions positively correlates with disorder. This suggests that internal functional groups can lead to disruptions in the graphitic lattice, causing somewhat weaker but broader UV-Vis spectra. Finally, the density of energy levels near the Fermi energy could help to explain the excitation dependent PL observed in some CNDs.

References

1. Xu, X.; Ray, R.; Gu, Y.; Ploehn, H. J.; Gearheart, L.; Raker, K.; Scrivens, W. A., Electrophoretic Analysis and Purification of Fluorescent Single-Walled Carbon Nanotube Fragments. *Journal of the American Chemical Society* **2004,** *126* (40), 12736-12737.

2. Cao, L.; Wang, X.; Meziani, M. J.; Lu, F.; Wang, H.; Luo, P. G.; Lin, Y.; Harruff, B. A.; Veca, L. M.; Murray, D.; Xie, S.-Y.; Sun, Y.-P., Carbon Dots for Multiphoton Bioimaging. *J. Am. Chem. Soc.* **2007,** *129* (37), 11318-11319.

3. Bhunia, S. K.; Saha, A.; Maity, A. R.; Ray, S. C.; Jana, N. R., Carbon nanoparticle-based fluorescent bioimaging probes. *Sci. Rep.* **2013,** *3*, 1473.

4. Liang, Q.; Ma, W.; Shi, Y.; Li, Z.; Yang, X., Easy synthesis of highly fluorescent carbon quantum dots from gelatin and their luminescent properties and applications. *Carbon* **2013,** *60*, 421-428.

5. Liu, Y.; Xiao, N.; Gong, N.; Wang, H.; Shi, X.; Gu, W.; Ye, L., One-step microwave-assisted polyol synthesis of green luminescent carbon dots as optical nanoprobes. *Carbon* **2014,** *68*, 258-264.

6. Du, J.; Xu, N.; Fan, J.; Sun, W.; Peng, X., Carbon Dots for In Vivo Bioimaging and Theranostics. *Small* **2019,** *15* (32), 1805087.

7. Singh, R. K.; Patel, K. D.; Mahapatra, C.; Kang, M. S.; Kim, H.-W., C-Dot Generated Bioactive Organosilica Nanospheres in Theranostics: Multicolor Luminescent and Photothermal Properties Combined with Drug Delivery Capacity. *ACS Applied Materials & Interfaces* **2016,** *8* (37), 24433-24444.

8. Feng, T.; Ai, X.; An, G.; Yang, P.; Zhao, Y., Charge-Convertible Carbon Dots for Imaging-Guided Drug Delivery with Enhanced in Vivo Cancer Therapeutic Efficiency. *ACS Nano* **2016,** *10* (4), 4410-4420.

9. Hettiarachchi, S. D.; Graham, R. M.; Mintz, K. J.; Zhou, Y.; Vanni, S.; Peng, Z.; Leblanc, R. M., Triple conjugated carbon dots as a nano-drug delivery model for glioblastoma brain tumors. *Nanoscale* **2019,** *11* (13), 6192-6205.

10. Ji, Z.; Sheardy, A.; Zeng, Z.; Zhang, W.; Chevva, H.; Allado, K.; Yin, Z.; Wei, J., Tuning the Functional Groups on Carbon Nanodots and Antioxidant Studies. *Molecules* **2019,** *24* (1).

11. Zeng, Z.; Zhang, W.; Arvapalli, D. M.; Bloom, B.; Sheardy, A.; Mabe, T.; Liu, Y.; Ji, Z.; Chevva, H.; Waldeck, D. H.; Wei, J., A fluorescence-electrochemical study of carbon nanodots (CNDs) in bio- and photoelectronic applications and energy gap investigation. *Phys Chem Chem Phys* **2017,** *19* (30), 20101-20109.

12. Zhang, W.; Chavez, J.; Zeng, Z.; Bloom, B.; Sheardy, A.; Ji, Z.; Yin, Z.; Waldeck, D. H.; Jia, Z.; Wei, J., Antioxidant Capacity of Nitrogen and Sulfur Codoped Carbon Nanodots. *ACS Applied Nano Materials* **2018,** *1* (6), 2699-2708.

13. Zeng, Z.; Zhang, W.; Arvapalli, D. M.; Bloom, B.; Sheardy, A.; Mabe, T.; Liu, Y.; Ji, Z.; Chevva, H.; Waldeck, D. H.; Wei, J., A fluorescence-electrochemical study of carbon nanodots (CNDs) in bio- and photoelectronic applications and energy gap investigation. *Phys. Chem. Chem. Phys.* **2017,** *19* (30), 20101-20109.

14. Mirtchev, P.; Henderson, E. J.; Soheilnia, N.; Yip, C. M.; Ozin, G. A., Solution phase synthesis of carbon quantum dots as sensitizers for nanocrystalline TiO_2 solar cells. *J. Mater. Chem.* **2012,** *22* (4), 1265-1269.

15. Tang, Q.; Zhu, W.; He, B.; Yang, P., Rapid Conversion from Carbohydrates to Large-Scale Carbon Quantum Dots for All-Weather Solar Cells. *ACS Nano* **2017,** *11* (2), 1540-1547.

16. Li, H.; Kang, Z.; Liu, Y.; Lee, S.-T., Carbon nanodots: synthesis, properties and applications. *Journal of Materials Chemistry* **2012,** *22* (46), 24230-24253.

17. Anwar, S.; Ding, H.; Xu, M.; Hu, X.; Li, Z.; Wang, J.; Liu, L.; Jiang, L.; Wang, D.; Dong, C.; Yan, M.; Wang, Q.; Bi, H., Recent Advances in Synthesis, Optical Properties, and Biomedical Applications of Carbon Dots. *ACS Appl. Bio Mater.* **2019,** *2* (6), 2317-2338.

18. Arcudi, F.; Đorđević, L.; Prato, M., Design, Synthesis, and Functionalization Strategies of Tailored Carbon Nanodots. *Acc. Chem. Res.* **2019,** *52* (8), 2070-2079.

19. Zhu, S.; Song, Y.; Zhao, X.; Shao, J.; Zhang, J.; Yang, B., The photoluminescence mechanism in carbon dots (graphene quantum dots, carbon nanodots, and polymer dots)-Current state and future perspective. *Nano Research* **2015,** *8* (2), 355-381.

20. Anilkumar, P.; Wang, X.; Cao, L.; Sahu, S.; Liu, J. H.; Wang, P.; Korch, K.; Tackett, K. N., 2nd; Parenzan, A.; Sun, Y. P., Toward quantitatively fluorescent carbon-based "quantum" dots. *Nanoscale* **2011,** *3* (5), 2023-7.

21. Sun, Y.; Wang, X.; Lu, F.; Cao, L.; Meziania, M. J.; Luo, P. G.; Gu, L.; Veca, L. M., Doped Carbon Nanoparticles as a New Platform for Highly Photoluminescent Dots. *J. Phys. Chem. C* **2008,** *112* (47), 18925-18928.

22. Deng, J.; Lu, Q.; Mi, N.; Li, H.; Liu, M.; Xu, M.; Tan, L.; Xie, Q.; Zhang, Y.; Yao, S., Electrochemical synthesis of carbon nanodots directly from alcohols. *Chem. Eur. J.* **2014,** *20* (17), 4993-9.

23. Hu, Q.; Paau, M. C.; Zhang, Y.; Chan, W.; Gong, X.; Zhang, L.; Choi, M. M., Capillary electrophoretic study of amine/carboxylic acid-functionalized carbon nanodots. *J. Chromatogr. A* **2013,** *1304*, 234-40.

24. Kalytchuk, S.; Polakova, K.; Wang, Y.; Froning, J. P.; Cepe, K.; Rogach, A. L.; Zboril, R., Carbon Dot Nanothermometry: Intracellular Photoluminescence Lifetime Thermal Sensing. *ACS Nano* **2017,** *11* (2), 1432-1442.

25. Meiling, T. T.; Schürmann, R.; Vogel, S.; Ebel, K.; Nicolas, C.; Milosavljević, A. R.; Bald, I., Photophysics and Chemistry of Nitrogen-Doped Carbon Nanodots with High Photoluminescence Quantum Yield. *The Journal of Physical Chemistry C* **2018,** *122* (18), 10217-10230.

26. Strauss, V.; Margraf, J. T.; Dolle, C.; Butz, B.; Nacken, T. J.; Walter, J.; Bauer, W.; Peukert, W.; Spiecker, E.; Clark, T.; Guldi, D. M., Carbon nanodots: toward a comprehensive understanding of their photoluminescence. *J. Am. Chem. Soc.* **2014,** *136* (49), 17308-16.

27. Li, Y.; Zhang, X.; Zheng, M.; Liu, S.; Xie, Z., Dopamine carbon nanodots as effective photothermal agents for cancer therapy. *RSC Adv.* **2016,** *6* (59), 54087-54091.

28. Wang, X.; Cao, L.; Lu, F.; Meziani, M. J.; Li, H.; Qi, G.; Zhou, B.; Harruff, B. A.; Kermarrec, F.; Sun, Y. P., Photoinduced electron transfers with carbon dots. *Chem. Commun.* **2009,** (25), 3774-6.

29. Li, Y.; Zhao, Y.; Cheng, H.; Hu, Y.; Shi, G.; Dai, L.; Qu, L., Nitrogen-doped graphene quantum dots with oxygen-rich functional groups. *J. Am. Chem. Soc.* **2012,** *134* (1), 15-8.

30. Dong, Y.; Pang, H.; Yang, H. B.; Guo, C.; Shao, J.; Chi, Y.; Li, C. M.; Yu, T., Carbon-based dots co-doped with nitrogen and sulfur for high quantum yield and excitation-independent emission. *Angew. Chem. Int. Ed.* **2013,** *52* (30), 7800-4.

31. Li, S.; Li, Y.; Cao, J.; Zhu, J.; Fan, L.; Li, X., Sulfur-doped graphene quantum dots as a novel fluorescent probe for highly selective and sensitive detection of Fe(3+). *Anal. Chem.* **2014,** *86* (20), 10201-7.

32. Omer, K. M.; Tofiq, D. I.; Hassan, A. Q., Solvothermal synthesis of phosphorus and nitrogen doped carbon quantum dots as a fluorescent probe for iron(III). *Microchimica Acta* **2018,** *185* (10), 466.

33. Jin, S. H.; Kim, D. H.; Jun, G. H.; Hong, S. H.; Jeon, S., Tuning the Photoluminescence of Graphene Quantum Dots through the Charge Transfer Effect of Functional Groups. *ACS Nano* **2013,** *7* (2), 1239-1245.

34. Casida, M. E.; Jamorski, C.; Casida, K. C.; Salahub, D. R., Molecular excitation energies to high-lying bound states from time-dependent density-functional response theory: Characterization and correction of the time-dependent local density approximation ionization threshold. *The Journal of Chemical Physics* **1998,** *108* (11), 4439-4449.

35. Gonze, X., A brief introduction to the ABINIT software package. *Z. Kristallogr. Cryst. Mater.* **2005,** *220* (5/6), 558.

36. Gonze, X.; Amadon, B.; Anglade, P. M.; Beuken, J. M.; Bottin, F.; Boulanger, P.; Bruneval, F.; Caliste, D.; Caracas, R.; Côté, M.; Deutsch, T.; Genovese, L.; Ghosez, P.; Giantomassi, M.; Goedecker, S.; Hamann, D. R.; Hermet, P.; Jollet, F.; Jomard, G.; Leroux, S.; Mancini, M.; Mazevet, S.; Oliveira, M. J. T.; Onida, G.; Pouillon, Y.; Rangel, T.; Rignanese, G. M.; Sangalli, D.; Shaltaf, R.; Torrent, M.; Verstraete, M. J.; Zerah, G.; Zwanziger, J. W., ABINIT: First-principles approach to material and nanosystem properties. *Computer Physics Communications* **2009,** *180* (12), 2582-2615.

37. Gonze, X.; Beuken, J. M.; Caracas, R.; Detraux, F.; Fuchs, M.; Rignanese, G. M.; Sindic, L.; Verstraete, M.; Zerah, G.; Jollet, F.; Torrent, M.; Roy, A.; Mikami, M.; Ghosez, P.; Raty, J. Y.; Allan, D. C., First-principles computation of material properties: the ABINIT software project. *Computational Materials Science* **2002,** *25* (3), 478-492.

38. Gonze, X.; Jollet, F.; Abreu Araujo, F.; Adams, D.; Amadon, B.; Applencourt, T.; Audouze, C.; Beuken, J. M.; Bieder, J.; Bokhanchuk, A.; Bousquet, E.; Bruneval, F.; Caliste, D.; Côté, M.; Dahm, F.; Da Pieve, F.; Delaveau, M.; Di Gennaro, M.; Dorado, B.; Espejo, C.; Geneste, G.; Genovese, L.; Gerossier, A.; Giantomassi, M.; Gillet, Y.; Hamann, D. R.; He, L.; Jomard, G.; Laflamme Janssen, J.; Le Roux, S.; Levitt, A.; Lherbier, A.; Liu, F.; Lukačević, I.; Martin, A.; Martins, C.; Oliveira, M. J. T.; Poncé, S.; Pouillon, Y.; Rangel, T.; Rignanese, G. M.; Romero, A. H.; Rousseau, B.; Rubel, O.; Shukri, A. A.; Stankovski, M.; Torrent, M.; Van Setten, M. J.; Van Troeye, B.; Verstraete, M. J.; Waroquiers, D.; Wiktor, J.; Xu, B.; Zhou, A.; Zwanziger, J. W., Recent developments in the ABINIT software package. *Computer Physics Communications* **2016,** *205*, 106-131.

39. Cuesta, A.; Dhamelincourt, P.; Laureyns, J.; Martínez-Alonso, A.; M. D. Tascón, J., Comparative performance of X-ray diffraction and Raman microprobe techniques for the study of carbon materials. *Journal of Materials Chemistry* **1998,** *8* (12), 2875-2879.

40. Kumar, S.; Ojha, A. K.; Ahmed, B.; Kumar, A.; Das, J.; Materny, A., Tunable (violet to green) emission by high-yield graphene quantum dots and exploiting its unique

properties towards sun-light-driven photocatalysis and supercapacitor electrode materials. *Materials Today Communications* **2017,** *11*, 76-86.

41. Merlen, A.; Buijnsters, J.; Pardanaud, C., A Guide to and Review of the Use of Multiwavelength Raman Spectroscopy for Characterizing Defective Aromatic Carbon Solids: from Graphene to Amorphous Carbons. *Coatings* **2017,** *7* (10), 153.

42. Sk, M. A.; Ananthanarayanan, A.; Huang, L.; Lim, K. H.; Chen, P., Revealing the tunable photoluminescence properties of graphene quantum dots. *J. Mater. Chem. C* **2014,** *2* (34), 6954-6960.

43. Geethalakshmi, K. R.; Ng, T. Y.; Crespo-Otero, R., Tunable optical properties of OH-functionalised graphene quantum dots. *Journal of Materials Chemistry C* **2016,** *4* (36), 8429-8438.

44. Li, F.; Liu, C.; Yang, J.; Wang, Z.; Liu, W.; Tian, F., Mg/N double doping strategy to fabricate extremely high luminescent carbon dots for bioimaging. *RSC Advances* **2014,** *4* (7), 3201-3205.

45. Fu, M.; Ehrat, F.; Wang, Y.; Milowska, K. Z.; Reckmeier, C.; Rogach, A. L.; Stolarczyk, J. K.; Urban, A. S.; Feldmann, J., Carbon Dots: A Unique Fluorescent Cocktail of Polycyclic Aromatic Hydrocarbons. *Nano Lett* **2015,** *15* (9), 6030-5.

46. Xu, X.; Liu, C.; Sun, Z.; Cao, T.; Zhang, Z.; Wang, E.; Liu, Z.; Liu, K., Interfacial engineering in graphene bandgap. *Chemical Society Reviews* **2018,** *47* (9), 3059-3099.

CHAPTER III

NOVEL MICROWAVE SYNTHESIS OF NEAR-METALLIC COPPER SULFIDE NANODISCS WITH SIZE CONTROL: EXPERIMENTAL AND DFT STUDIES OF CHARGE CARRIER DENSITY

This chapter has been published as: A. T. Sheardy, D. M. Arvapalli and J. Wei, *Nanoscale Adv.*, 2020, **2**, 1054. **DOI:** 10.1039/D0NA00069H - Published by The Royal Society of Chemistry
https://pubs.rsc.org/en/content/articlelanding/2020/na/d0na00069h#!divAbstract

Introduction

Copper sulfide (Cu_xS, $1 \leq x \leq 2$) nanoparticles have recently been the focus of a variety of optical-based studies, including: bioimaging/detection,[1, 2] photothermal therapy,[3, 4] photovoltaics,[11] and photocatalysis.[12, 13] The majority of these studies are based on the plasmonic near-infrared absorption band, which has been explicitly studied both experimentally[9, 14, 15] and theoretically.[16-18] The plasmon absorption arises from intrinsic p-doping that is dependent on the stoichiometric ratio of Cu:S; increased sulfur content results in increased p-doping and therefore a stronger and higher energy plasmon absorption.[5, 6, 9, 19-24] This results in more controllability of the plasmon in comparison to traditional noble metal nanoparticles, as the charge carrier density can be modified in semiconductor plasmons in addition to size and morphology.[25] Stoichiometric CuS (x=1, covellite) is the most heavilydoped of the copper sulfides, thus exhibiting the

strongest plasmon absorption and of the most interest for these potential applications.[14, 15]

Despite the myriad potential applications for CuS NPs, most of the syntheses used are not ideal for wide-spread use. A summary of some of the various synthetic methods used to synthesize Cu_xS NPs of varying stoichiometry is gathered in Table B.S1. Many of these reactions require temperatures on the order of 150-200 °C and/or multistep preparation of precursors. Some hydrothermal syntheses at lower temperature (90 °C) have been performed, but the concentration used in these reactions was 1 mM, making this prohibitive for commercial applications. Copper sulfide NPs have been synthesized using microwave synthesis, however micron-sized particles with nanoscale features have been generally reported. Kim *et al.* synthesized 13 nm CuS nanodiscs, but the procedure required multiple steps and the reaction was not explored in depth.[20]

Microwave synthesis is an emerging technique used in both organic[31] and inorganic[32] synthesis that could potentially replace conventional heating in many processes and allow for more efficient synthesis. Microwave-assisted synthetic methods show many advantages over traditional heating, including reduced reaction times, faster/more uniform heating, increased reproducibility, and simpler reaction setups. In a simple sense, microwave heating functions by causing molecular rotations which result in molecular friction and therefore heat. Further, since the microwaves can penetrate through the solvent, heating can occur in the entire reaction simultaneously, vs. conventional heating which is dependent on

external heating and stirring to achieve thermal equilibrium. Finally, traditional heating methods can require high temperatures and techniques like hot injection to achieve reproducible nanoparticle size, but the rapid heating of microwave reactions eliminates the need for complicated synthetic techniques.[26-27] For these reasons, we aim to provide a more comprehensive study on the microwave synthesis of plasmonic CuS nanoparticles.

Table 3.1. Summary of Data Used for Charge Carrier Density Calculation.

Time (min)	**Diameter (nm)**	**Height (nm)**	**L_x**	**λ (nm)**	**γ (eV)**	**$\hbar\omega_{sp}$ (eV)**	**$\hbar\omega_p$ (eV)**	**n_h (10^{22} cm^{-3})**
5	6.5 ± 1.9	3.3 ± 0.5	0.239	1176 ± 2.6	0.461	1.05	4.65	1.25
10	8.5 ± 2.3	4.2 ± 0.7	0.235	1197 ± 7.6	0.454	1.04	4.62	1.24
15	11.6 ± 3.2	4.5 ± 0.7	0.202	1215 ± 27.5	0.411	1.02	4.92	1.41

Further, while many of the proposed applications for CuS NPs are based on the electronic properties of the NPs, these properties remain poorly treated. As mentioned above, copper sulfides are intrinsically p-doped, meaning the charge carriers are mainly holes. The density of charge carriers is of particular interest, as it affects both the energy of the plasmon and the conductivity. Calculation of the charge carrier density is often performed using the Drude model (Eq. 3.1-2, see discussion), which has dependence on both the shape of the nanoparticle and the effective mass of the charge carriers.[7, 9, 15, 20, 23, 24] Often in literature, the shape factor is assumed to be that of a spherical particle (L = 1/3), regardless of the actual shape of the particle. The effective mass of holes in Cu_2S has been reported in literature as $0.8m_e$,[18] however the effective mass for stoichiometric CuS has not

been theoretically studied and rather is assumed to be the same as Cu_2S. This assumption is unlikely valid based on the results of the computational study by Lukashev *et al.*, which shows that Cu_2S is a traditional semiconductor, while the introduction of additional sulfur atoms introduces more metallic character.[18] A review by Kriegel *et al.* on plasmonic semiconductors presents an experimentally reported CuS effective mass of $0.55m_e$, however these experiments were based on an experimental study of $Ba_{1-x}K_xCuSF$, making it erroneous to attribute this value to pure CuS.[6, 19, 28] As such, the authors are unaware of any experimental or theoretical studies that have determined the effective mass for carriers in pure stoichiometric CuS. For these reasons, we have combined experimental results with density functional theory (DFT)-calculated results to better determine both an experimental and theoretical charge carrier density in CuS nanoparticles, along with an appropriate effective mass for the charge carriers.

Experimental

CuS Nanoparticle Synthesis

The synthesis of the CuS NPs was based on a variation of the method used by Lee *et al*, who used conventional heating to synthesize Cu_2S.[11] A solution of 33 mg copper acetylacetonate ($Cu(acac)_2$, 0.125 mmol) in 10 mL slightly heated oleylamine was prepared in a 25 mL round bottom flask. To this solution, 4 mg elemental sulfur (S, 0.125 mmol) was added. The flask was then alternatingly purged with vacuum and nitrogen to remove any oxygen, transferred to a microwave synthesizer (CEM Discover) and microwaved at 150 W for 5, 10, or 15 minutes, with low stirring. The resulting

solution was then rapidly air-cooled and ethanol was added to help precipitate the NPs. The particles were collected by centrifugation at 10000 RPM for 10 minutes. For characterizations requiring solutions, the particles were easily resuspended in chloroform.

Characterization

Transmission electron microscopy (TEM, Zeiss Libra 120 Plus) was used to determine the size and shape of the resulting NPs. The asymmetrical nature of the synthesized particles required two methods for preparing TEM samples. Simply drop casting chloroform-dispersed NPs directly on a TEM grid resulted in particles mostly assembling parallel to the support film. Alternatively, Hsu *et al.* presented a method of allowing a droplet of chloroform-dispersed NPs to float and dry at an air-water interface prior to transferring to a TEM grid, resulting in many particles assembling perpendicular to the support film.[1] Crystallinity was assessed by x-ray diffraction (XRD) using a Cu source (Agilent Gemini), optical properties were measured by UV-Vis-NIR spectroscopy (Varian Cary 6000i), and stoichiometry was determined by x-ray photoelectron spectroscopy (XPS, Thermo Scientific Escalab Xi+). Fourier transform infrared spectroscopy (FTIR, Varian 670) was used to confirm the presence of the oleylamine capping agent, and thermogravimetric analysis (TGA, TA Instruments Q-500) was performed under N_2 to determine the amount of capping agent.

Density Functional Theory Calculations

Density functional theory (DFT) calculations of the total energy, density of states, and band structure were calculated using Quantum Espresso,[31] following the methodology of Morales-Garcia *et al.*[16] Specifically, the calculations were

performed using the generalized gradient approximation (GGA), with a projector-augment wave (PAW) all-electron description[32-33] and Perdew, Burke, and Ernzerhof (PBE) exchange-correlation functional.[34] Calculations were performed using a Monkhorst-Pack[35] grid of k-points (10 x 10 x 2), with a plane-wave cutoff of 560 eV. For convergence, a consecutive total energy difference of less than 10^{-4} eV was required. Since DFT is known to underestimate the bandgap, the Dudarev simplified rotationally invariant form of DFT+U was used.[36] Values of *U* (6 eV) and *J* (1 eV) were chosen based on the results from Morales-Garcia *et al*, giving an effective *U* of 5 eV.[16]

Results and Discussion

TEM images of the synthesized CuS NPs are given in Figure 3.1 both parallel (A-C) and perpendicular (D-F) to the support film. As can be seen from the images, there is an obvious increase in the diameter of the particles with increasing reaction time, and multiple morphologies including circles, triangles and hexagons are present. The insets on Figure 3.1 show the electron diffraction pattern, indicating the crystalline nature of the particles. Specifically, the bright ring in all samples corresponds to the $(2\bar{1}0)$ plane, with a lattice spacing of 1.88 Å. From Figure 3.1D-F, it can be seen that the particles are discs, which is consistent with the expected hexagonal crystal structure. Size distributions for both the diameter and height of The particles are given in Fig B.S1, and there is a clear increase in both dimensions with increasing reaction time. The size data is also summarized in Table 3.1.

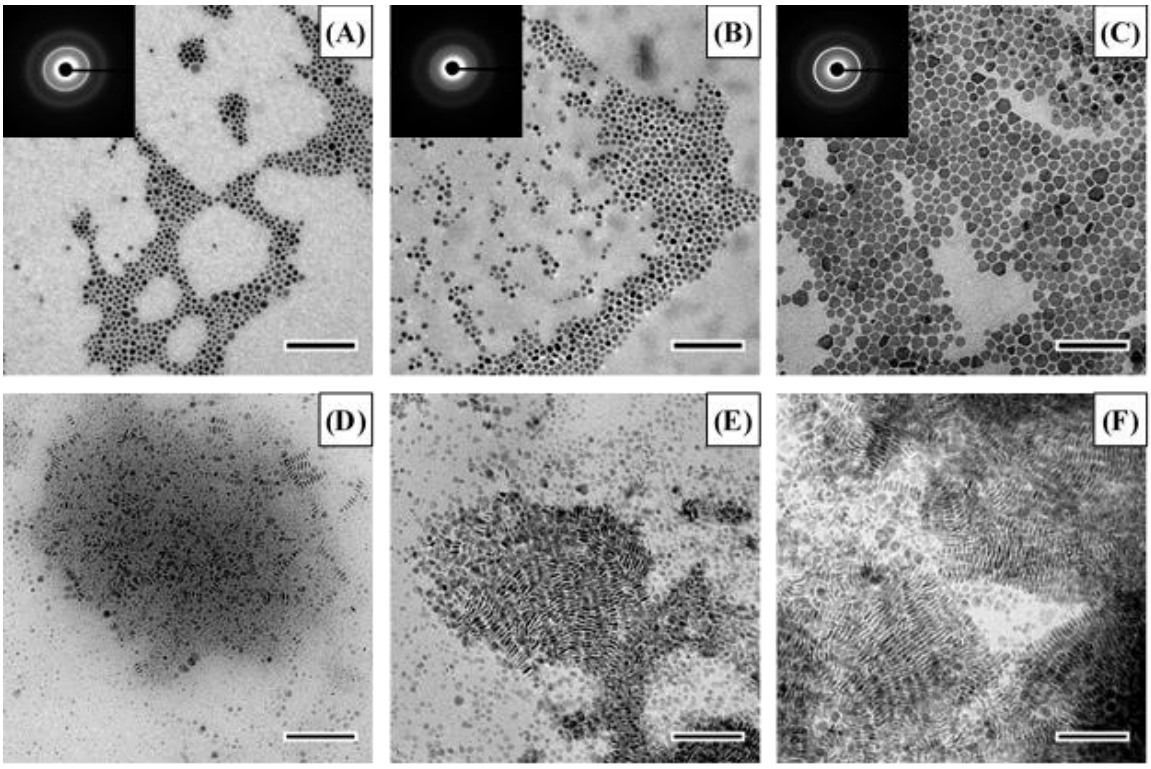

Figure 3.1. TEM of CuS NPs. Representative TEM micrographs of CuS NPs synthesized for 5 (A,D), 10 (B,E), or 15 (C,F) minutes either parallel (A-C) or perpendicular (D-F) to the carbon support film. The insets on the micrographs show the electron diffraction pattern, and the scale bar on all images is 100 nm.

FTIR spectroscopy was used to confirm the presence of the oleylamine capping agent (Fig B.S2A), and the agreement between pure oleylamine and the CuS NPs can be clearly seen. TGA between 100-800 °C shows similar structure between all reaction times, with two main mass losses at ~250 and ~450 °C (Fig B.S2B). The first of these losses corresponds to ~30% of the mass and is due to the loss of sulfur and formation of higher copper stoichiometries.[29] The second loss is approximately 40% of the initial mass and is attributed to the loss of the oleylamine capping agent. XPS was performed to verify the expected 1:1

stoichiometry for CuS (Fig B.S2C). From these experiments, the major elements present are copper, sulfur, carbon, nitrogen, and oxygen. The carbon and nitrogen are expected from the oleylamine capping agent, while the oxygen may be due to surface contamination. Table B.S2 lists the Cu and S content for each sample, and the materials do present an approximate 1:1 relationship. The relatively low elemental content of each of these elements (2-8% each) and deviations from 1:1 stoichiometry are due to a high carbon content (~75-80%) from the capping agent and the relatively shallow probe depth of the technique. High resolution scans of the Cu L-edge give a single peak for the p3/2 signal at ~933.3 eV and a single peak for the p1/2 signal at ~953.1 eV (Fig. B.S3D). For the S L-edge, a single peak at ~163.5 eV is observed (Fig. B.S3E).

X-Ray Diffraction was performed to verify that the crystal structure of the synthesized nanodiscs matches the expected structure for stoichiometric CuS (Fig B.S3). As can be seen, the experimental data for all synthesized samples show good agreement with the predicted diffraction pattern shown in black. Taken together the FTIR, TGA, XRD and XPS data confirm the synthesis of stoichiometric CuS capped with oleylamine, with no major differences between different reaction times, excepting size/aspect ratio.

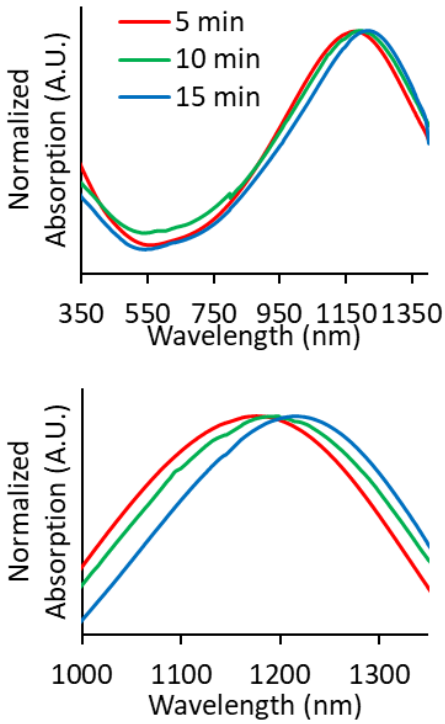

Figure 3.2. UV-VIS of CuS NPs. UV-Vis-NIR absorption spectra of CuS synthesized with reaction times of 5 (Red), 10 (Green), and 15 minutes (Blue). The spectra have been normalized for comparison, and both the entire spectra (top) and plasmon absorption (bottom) are shown. The peak absorptions occur at 1176, 1197, and 1215 nm, respectively.

UV-Vis-NIR spectra were measured (Figure 3.2), and it can be seen that there is a red shift of the NIR plasmon peak with increasing reaction time. Based on this plasmon peak, it is possible to calculate the density of charge carriers (holes), n_h, according to the Drude model and Eqs. 3.1-2. [7, 9, 15, 20, 23, 24] In these equations, ω_{sp} is the surface plasmon frequency, ω_p is the bulk plasmon frequency, ε_m is the dielectric constant of the media ($CHCl_3$, 4.81), γ is the plasmon linewidth, L is the shape factor, e is the charge of an electron, m_h is the effective mass of the holes, and ε_0 is the free space permittivity. In the

calculations that follow, ω_{sp} and γ are taken from the position and FWHM of the plasmon resonance, respectively. The shape factor for an oblate ellipsoid can be found using Eq. 3.3, and for disc-like particles it is assumed that $L_x = L_y < L_z$ ($r_1 = r_2 < r_3$).[30] Finally, an effective hole mass of $0.8m_e$ was used, based on previous literature.[9, 24] These calculations result in hole densities of 1.25, 1.24, and 1.41 × 10^{22} cm^{-3} for 5, 10 and 15 minute reactions, respectively. For comparison, gold and copper have electron densities of 5.9 and 8.4 × 10^{22} cm^{-3}, respectively, so the charge carrier densities of synthesized CuS NPs approach near-metallic levels of charge carriers. All of the data used in these calculations is summarized in Table 3.1.

$$\omega_{sp} = \sqrt{\frac{{\omega_p}^2}{1 + \left(\frac{1}{L} - 1\right)\varepsilon_m} - \gamma^2} \tag{3.1}$$

$$\omega_p = \sqrt{\frac{n_h e^2}{m_h \varepsilon_0}} \tag{3.2}$$

$$L_i = \frac{r_1 r_2 r_3}{2} \int_0^\infty \frac{ds}{(s + {r_i}^2)\sqrt{(s + {r_1}^2)(s + {r_2}^2)(s + {r_3}^2)}} \tag{3.3}$$

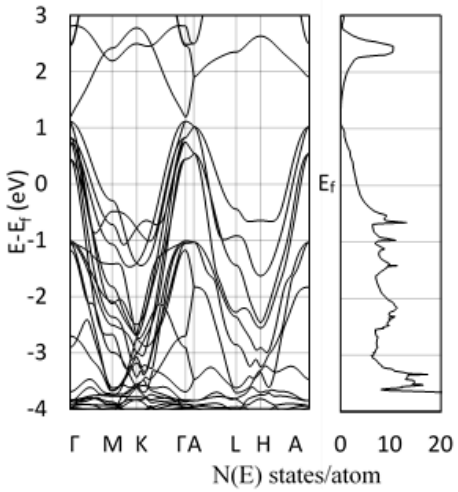

Figure 3.3. Calculated Band Structure and Density of States for CuS. DFT-calculated band structure (left) and density of states (right) using DFT+U (Ueff=5). Energies are relative to the Fermi energy, and both figures share the same y-axis values.

A number of different copper sulfide stoichiometries have been studied in terms of the carrier effective mass, charge carrier density, and band gap; these data have been collected in Table 3.2. Cu_2S has been shown to be purely semiconducting, and therefore has insufficient charge carriers to support a plasmon.[9, 18] Increasing sulfur content results in increased charge carrier densities, with the charger carrier density for CuS being approximately one order of magnitude higher than the less heavily doped stoichiometries. Specifically, previous literature has reported CuS hole densities in the range of $0.5 – 1.6 \times 10^{22}$ cm^{-3}, of similar order to those report in this work.[5, 6, 20-24] It should be noted that most of these calculations are dependent on the effective mass of the charge carriers (holes), but these values have only been computationally reported for Cu_2S, and other studies assume that the mass does not change significantly. The near-metallic nature of CuS[23] suggests that the effective mass of the carrier should

be different than that of purely semiconducting Cu_2S. For this, values of 0.55, 0.8, and $1m_e$ have been used, but the former of these comes from an experiment using $Ba_{1-x}K_xCuSF$,[19] while the latter values are assumptions.

Table 3.2. Summary of Previous Electronic Properties for Cu_xS. Summary of previously used/reported values for carrier effective mass, charge carrier density and band gap for multiple $Cu_{2-x}S$ stoichiometries. The results from this work are also included.

Stoichiometry	**Carrier Effective Mass (m_e)**	**Charge Carrier Density (cm^{-3})**	**Band Gap (eV)**
Cu_2S[5, 14]	0.8	-	0.6, 2.4
$Cu_{1.94}S$ – $Cu_{1.98}S$[5-10]	0.8	$0.7 – 1.3 \times 10^{21}$	1.53
$Cu_{1.94}S$ – $Cu_{1.8}S$ (Theoretical)[18]	-	$0.8 – 2.4 \times 10^{21}$	0.55
$Cu_{1.8}S$[5, 6, 10]	0.8	$3.0 – 4.6 \times 10^{21}$	1.46, 2.55
$Cu_{1.4}S$[5, 21]	0.8	5.88×10^{21}	2.5
CuS[5, 6, 10, 20-24]	0.55-1	$0.5 – 1.6 \times 10^{22}$	1.48, 2.58
CuS (This work)	0.3	9.8×10^{21} (Theoretical) $4.7\text{-}5.27 \times 10^{21}$ (Experimental)	N/A

In order to verify the experimental charge carrier density, a density functional theory (DFT) calculation of the band structure and density of states (DOS) was performed (Figure 3.3), following the methodology of Morales-Garcia *et al.* [16] Using DFT+U, the band structure and DOS of bulk CuS were calculated (Figure 3.3) and show good agreement with Morales-Garcia's calculations. From simple solid state physics, the number of charge carriers (N) is given by Eq. 3.4, where $f(E)$ is the Fermi-Dirac distribution and $g(E)$ is the density of states.[37] At 0 K, the Fermi-Dirac distribution for holes would simplify to either 0 ($E < E_f$) or 1 ($E > E_f$). While this assumption is only completely accurate at 0 K, at higher temperatures the distribution of charge carriers will change, but the total density

should remain relatively unchanged. Further, seeing as the Fermi energy is within the conduction band, only the holes within that same band are likely to contribute to charge carrying in the plasmon, as holes in higher bands would be too high energy. Taking these assumptions together, Eq. 3.4 can be simplified to Eq. 3.5, where E_c is the top of the conduction band and V is the unit cell volume. Performing this calculation results in a calculated ~2 holes per unit cell, or n_h = 9.81×10^{21} cm^{-3}. This computationally derived result shows good agreement both with previous literature and the present results. Specifically, the value of two holes per unit cell is consistent with the prediction of Conejeros *et al*., based on the expected number of electrons and the number of states available.[38] Work by Mazin also shows similar results of 1/3 of a hole per Cu, combined with the 6 copper atoms per unit cell gives a total of two holes per unit cell.[39]

$$N(E) = \int f(E)g(E)dE \tag{3.4}$$

$$n_h V = N_h = \int_{E_f}^{E_c} g(E)dE \tag{3.5}$$

The DFT-calculated charge density is of similar order, but slightly lower than the experimentally calculated value. One likely source for this discrepancy is an over-estimation of the value of γ, due to experimental broadening of the peak. Additionally, the dielectric constant used was for chloroform, while the oleylamine capping agent likely changes the effective dielectric constant around the NPs.

Finally, the largest source of discrepancy between experiment and theory could come from the choice of the effective hole mass as $0.8m_e$. As previously discussed, the prior reported values for the hole mass in CuS do not come from pure samples, or is assumed to be the same as Cu_2S. For this reason, the effective hole mass was calculated in the Γ-M direction around the Fermi energy using Eq. 3.6. Performing this calculation results in an effective hole mass of $0.3m_e$. The Γ-M direction was selected based both on the work of Lukashev *et al.*[18] and the fact that this represents the same transverse direction the plasmon oscillates in. To ensure that there were no significantly different effective masses, the Γ-K direction was also tested. The calculated effective mass is consistent with Lukashev's calculated electron effective mass for Cu_2S, a result that is not unexpected. For a metal at reasonable temperatures, the narrow spread of the Fermi-Dirac distribution should result in electrons and holes having similar effective masses. Using this effective mass results in experimental charge carrier densities of 4.70, 4.64 and 5.27×10^{21} cm^{-3}, which are approximately half of the predicted value of 9.81×10^{21} cm^{-3}. This effective mass can be considered as a lateral effective mass; the transverse effective mass calculated at the Γ point using the Γ-A direction is significantly larger with $m_h^*=3.7m_e$ and $m_e^*=0.83m_e$. Combined with a calculated energy gap of 1.45 eV in the z-direction, it is not expected that there will be sufficient carriers with small enough effective mass to support an out-of-plane plasmon. The band structures in the Γ-A and Γ-M direction used for these calculations can be found in Fig. B.S4.

$$E = \frac{\hbar^2 k^2}{2m_h} \tag{3.6}$$

Conclusion

In conclusion, a new simple size-controlled microwave synthesis method for oleylamine-capped CuS nanodiscs has been developed. The particles have undergone multiple characterization techniques to accurately determine the structure and confirm that the only differences made by reaction time are the size of the disc-like NPs and resulting plasmon absorption. Further, using a conventional effective hole mass of $0.8m_e$, charge carrier densities 1.2-1.4 × 10^{22} cm^{-3} were obtained, while density functional theory was used to determine a predicted charge carrier density of 9.81 × 10^{21} cm^{-3}. Using the calculated band structure around the Fermi energy resulted in a lower effective hole mass of $0.3m_e$, closer to that predicted for electrons in less heavily doped copper sulfides. Finally, using this calculated effective mass, the experimental charge carrier densities were recalculated as 4.7-5.3 × 10^{21} cm^{-3}, approximately half of the predicted value.

References

1. Ding, K.; Zeng, J.; Jing, L.; Qiao, R.; Liu, C.; Jiao, M.; Li, Z.; Gao, M., Aqueous synthesis of PEGylated copper sulfide nanoparticles for photoacoustic imaging of tumors. Nanoscale 2015, 7 (25), 11075-81.

2. Ku, G.; Zhou, M.; Song, S.; Huang, Q.; Hazle, J.; Li, C., Copper Sulfide Nanoparticles As a New Class of Photoacoustic Contrast Agent for Deep Tissue Imaging at 1064 nm. ACS Nano 2012, 6 (8), 7489-6496.

3. Zhou, M.; Li, J.; Liang, S.; Sood, A. K.; Liang, D.; Li, C., CuS Nanodots with Ultrahigh Efficient Renal Clearance for Positron Emission Tomography Imaging and Image-Guided Photothermal Therapy. ACS Nano 2015, 9 (7), 7085-96.

4. Zhou, M.; Zhang, R.; Huang, M.; Lu, W.; Song, S.; Melancon, M. P.; Tian, M.; Liang, D.; Li, C., A Chelator-Free Multifunctional (64Cu)CuS Nanoparticle Platform for Simultaneous Micro-PET-CT Imaging and Photothermal Ablation Therapy. J Am Chem Soc 2010, 132, 15351-15358.

5. Grozdanov, I.; Najdoski, M., Optical and Electrical Properties of Copper Sulfide Films of Variable Composition. Journal of Solid State Chemistry 1995, 114 (2), 469-475.

6. Hsu, S. W.; Ngo, C.; Tao, A. R., Tunable and directional plasmonic coupling within semiconductor nanodisk assemblies. Nano Lett 2014, 14 (5), 2372-80.

7. Hsu, S.-W.; Bryks, W.; Tao, A. R., Effects of Carrier Density and Shape on the Localized Surface Plasmon Resonances of Cu2–xS Nanodisks. Chemistry of Materials 2012, 24 (19), 3765-3771.

8. Hsu, S.-W.; On, K.; Tao, A. R., Localized Surface Plasmon Resonances of Anisotropic Semiconductor Nanocrystals. Journal of the American Chemical Society 2011, 133 (47), 19072-19075.

9. Luther, J. M.; Jain, P. K.; Ewers, T.; Alivisatos, A. P., Localized surface plasmon resonances arising from free carriers in doped quantum dots. Nat Mater 2011, 10 (5), 361-6.

10. Parreira, P.; Lavareda, G.; Amaral, A.; Botelho do Rego, A. M.; Conde, O.; Valente, J.; Nunes, F.; Nunes de Carvalho, C., Transparent p-type CuxS thin films. Journal of Alloys and Compounds 2011, 509 (16), 5099-5104.

11. Lee, H.; Yoon, S. W.; Kim, E. J.; Park, J., In-Situ Growth of Copper Sulfide Nanocrystals on Multiwalled Carbon Nanotubes and Their Application as Novel Solar Cell and Amperometric Glucose Sensor Materials. Nano Lett 2007, 7 (3), 778-784.

12. Kim, Y.; Park, K. Y.; Jang, D. M.; Song, Y. M.; Kim, H. S.; Cho, Y. J.; Myung, Y.; Park, J., Synthesis of Au-Cu2S Core-Shell Nanocrystals and Their Photocatalytic and Electrocatalytic Activity. J Phys Chem C 2010, 114, 22141-22146.

13. Ratanatawanate, C.; Bui, A.; Vu, K.; Balkus, K. J., Low-Temperature Synthesis of Copper(II) Sulfide Quantum Dot Decorated TiO2Nanotubes and Their Photocatalytic Properties. The Journal of Physical Chemistry C 2011, 115 (14), 6175-6180.

14. Brelle, M. C.; Lorres-Martinez, C. L.; McNulty, J. C.; Mehra, R. K.; Zhang, J. Z., Synthesis and characterization of CuXS nanoparticles. Nature of the infrared band and charge-carrier dynamics. Pure Appl. Chem. 2000, 72 (1-2), 101-117.

15. Zhao, Y.; Pan, H.; Lou, Y.; Qui, X.; Zhu, J.; Burda, C., Plasmonic Cu(2-x)S Nanocrystals - Optical and Structural Properties of Copper-Deficient Copper (I) Sulfides. J Am Chem Soc 2009, 131, 4253-4261.

16. Morales-Garcia, A.; Soares, A. L., Jr.; Dos Santos, E. C.; de Abreu, H. A.; Duarte, H. A., First-principles calculations and electron density topological analysis of covellite (CuS). J Phys Chem A 2014, 118 (31), 5823-31.

17. Xiao, L.; Wu, J.; Ran, J.; Liu, Y.; Qiu, W.; Lu, F.; Shao, F.; Tang, D.; Peng, P., Near-infrared radiation absorption properties of covellite (CuS) using first-principles calculations. AIP Advances 2016, 6 (8), 085122.

18. Lukashev, P.; Lambrecht, W. R. L.; Kotani, T.; van Schilfgaarde, M., Electronic and crystal structure of Cu2-xS: Full-potential electronic structure calculations. Physical Review B 2007, 76 (19), 195202.

19. Kykyneshi, R. Pulsed Laser Deposition and Thin Film Properties of p-type BaCuSF, BaCuSeF, BaCuTeF and n-type Zn2In2O5 Wide Band-Gap Semiconductors. Dissertation, Oregon State University, 2007.

20. Kim, M. R.; Hafez, H. A.; Chai, X.; Besteiro, L. V.; Tan, L.; Ozaki, T.; Govorov, A. O.; Izquierdo, R.; Ma, D., Covellite CuS nanocrystals: realizing rapid microwave-

assisted synthesis in air and unravelling the disappearance of their plasmon resonance after coupling with carbon nanotubes. Nanoscale 2016, 8 (26), 12946-57.

21. Liu, L.; Zhong, H.; Bai, Z.; Zhang, T.; Fu, W.; Shi, L.; Xie, H.; Deng, L.; Zou, B., Controllable Transformation from Rhombohedral Cu1.8S Nanocrystals to Hexagonal CuS Clusters: Phase- and Composition-Dependent Plasmonic Properties. Chemistry of Materials 2013, 25 (23), 4828-4834.

22. Liu, M.; Xue, X.; Ghosh, C.; Liu, X.; Liu, Y.; Furlani, E. P.; Swihart, M. T.; Prasad, P. N., Room-Temperature Synthesis of Covellite Nanoplatelets with Broadly Tunable Localized Surface Plasmon Resonance. Chemistry of Materials 2015, 27 (7), 2584-2590.

23. Xie, Y.; Carbone, L.; Nobile, C.; Grillo, V.; D'Agostino, S.; Sala, F. D.; Giannini, C.; Altamura, D.; Oelsner, C.; Kryschi, C.; Cozzoli, P. D., Metallic-like Stoichiometric Copper Sulfide Nanocrystals: Phase- and Shape-Selective Synthesis, Near-Infrared Surface Plasmon Resonance Properties and Their Modeling. ACS Nano 2013, 7 (8), 7352-7369.

24. Xie, Y.; Riedinger, A.; Prato, M.; Casu, A.; Genovese, A.; Guardia, P.; Sottini, S.; Sangregorio, C.; Miszta, K.; Ghosh, S.; Pellegrino, T.; Manna, L., Copper sulfide nanocrystals with tunable composition by reduction of covellite nanocrystals with Cu+ ions. J Am Chem Soc 2013, 135 (46), 17630-7.

25. Jain, P. K.; Manthiram, K.; Engel, J. H.; White, S. L.; Faucheaux, J. A.; Alivisatos, A. P., Doped nanocrystals as plasmonic probes of redox chemistry. Angew Chem Int Ed Engl 2013, 52 (51), 13671-5.

26. Kappe, C. O., Controlled microwave heating in modern organic synthesis. Angew Chem Int Ed Engl 2004, 43 (46), 6250-84.

27. Bilecka, I.; Niederberger, M., Microwave chemistry for inorganic nanomaterials synthesis. Nanoscale 2010, 2 (8), 1358.

28. Kriegel, I.; Scotognella, F.; Manna, L., Plasmonic doped semiconductor nanocrystals: Properties, fabrication, applications and perspectives. Physics Reports 2017, 674, 1-52.

29. Godočíková, E.; Baláž, P.; Criado, J. M.; Real, C.; Gock, E., Thermal behaviour of mechanochemically synthesized nanocrystalline CuS. Thermochimica Acta 2006, 440 (1), 19-22.

30. Barnes, W. L., Particle plasmons: Why shape matters. American Journal of Physics 2016, 84 (8), 593-601.

31. Giannozzi, P.; Baroni, S.; Bonini, N.; Calandra, M.; Car, R.; Cavazzoni, C.; Ceresoli, D.; Chiarotti, G. L.; Cococcioni, M.; Dabo, I.; Dal Corso, A.; de Gironcoli, S.; Fabris, S.; Fratesi, G.; Gebauer, R.; Gerstmann, U.; Gougoussis, C.; Kokalj, A.; Lazzeri, M.; Martin-Samos, L.; Marzari, N.; Mauri, F.; Mazzarello, R.; Paolini, S.; Pasquarello, A.; Paulatto, L.; Sbraccia, C.; Scandolo, S.; Sclauzero, G.; Seitsonen, A. P.; Smogunov, A.; Umari, P.; Wentzcovitch, R. M., QUANTUM ESPRESSO: a modular and open-source software project for quantum simulations of materials. J Phys Condens Matter 2009, 21 (39), 395502.

32. Blöchl, P. E., Projector augmented-wave method. Physical Review B 1994, 50 (24), 17953-17979.

33. Kresse, G.; Joubert, D., From ultrasoft pseudopotentials to the projector augmented-wave method. Physical Review B 1999, 59 (3), 1758-1775.

34. Perdew, J. P.; Burke, K.; Ernzerhof, M., Generalized Gradient Approximation Made Simple. Physical Review Letters 1996, 77 (18), 3865-3868.

35. Monkhorst, H. J.; Pack, J. D., Special points for Brillouin-zone integrations. Physical Review B 1976, 13 (12), 5188-5192.

36. Dudarev, S. L.; Botton, G. A.; Savrasov, S. Y.; Humphreys, C. J.; Sutton, A. P., Electron-energy-loss spectra and the structural stability of nickel oxide: An LSDA+U study. Physical Review B 1998, 57 (3), 1505-1509.

37. Kittel, C., Introduction to Solid State Physics, 8th Edition. Wiley: 2004.

38. Conejeros, S.; Moreira Ide, P.; Alemany, P.; Canadell, E., Nature of holes, oxidation states, and hypervalency in covellite (CuS). Inorg Chem 2014, 53 (23), 12402-6.

39. Mazin, I. I., Structural and electronic properties of the two-dimensional superconductor CuS with 1/3-valent copper. Physical Review B 2012, 85 (11), 115133.

CHAPTER IV

PHOTOTHERMAL EFFECT MEASUREMENT OF COPPER SULFIDE NANODISCS

Introduction

According to the National Cancer Institute, approximately 39.6% of people will be diagnosed with some form of cancer during their life.[1] While overall mortality in the United States has decreased, it is highly dependent on the type of cancer.[2] Further, the traditional treatments for cancer (surgery, radiation and chemotherapy) are invasive and can carry numerous side effects by damaging both healthy and cancerous cells.[3] For this reason, alternative treatments such as immunotherapy,[4] targeted chemotherapies,[3-4] and hyperthermia[5] are being explored. Hyperthermia, defined as raising cellular temperatures above 40 °C to induce apoptosis, is of particular interest, as it can be quite selective. However, standard hyperthermia treatment heats the entire body and is based on an increased heat susceptibility of cancer cells, or requires an invasive implantable probe for localized heating.[5] A more specialized treatment, photothermal therapy (PTT) is preferable as an external laser is used to heat nanoparticles within a tumor.[6] This results in a localized treatment without the need for any invasive procedures.

Photothermal therapy was first explored in 2003 by Hirsch *et al.* using gold nanoshell coated SiO_2 nanoparticles (NPs).[7] Since that time, gold particles of varied shapes have remained popular,[8-10] as have carbonaceous materials,[11-13] copper sulfide (CuS),[14-16]various hybrids containing noble metals and/or carbonaceous materials,[17-22]

and other miscellaneous materials.[23-27] The general procedure for this process is to target the NPs to a tumor and irradiate the sample with a 808 nm near infrared (NIR) laser. NPs will absorb the NIR light and convert the energy to heat via the photothermal effect (PTE). The resulting heat is enough to irreversibly damage the cells by inducing apoptosis via hyperthermia.[5] One of the keys to this approach is that biological tissues have low absorption of NIR photons, allowing for penetration depths of up to 3 cm.[28] However, while these particles are able to damage cancerous cells, Choi *et al*. have shown that particles larger than 5.5 nm are not efficiently cleared from the body post-treatment.[29] Table 4.1 presents a summary of some of the common particles tested and their two key properties; dimensions and optical absorption properties. As this data shows, most particles have at least one dimension larger than 5.5 nm, with the only exception being CuS NPs. Despite having an ideal size, the peak NIR absorption of these CuS NPs was at ~990 nm, a longer wavelength than that of the 808 nm laser being used to induce hyperthermia. Further, the synthesis of these particles required fairly dilute concentrations and thus present an obstacle towards industrial-scale synthesis.

Table 4.1. Summary of Materials Used for Photothermal Therapy.

Material	Size	Peak Absorption Wavelength
Gold Nanoshells[7]	120 nm (diameter)	820 nm
Gold Nanorods[8]	50 x 10 nm	800 nm
Carbon Nanotubes (SWCNT)[11]	150 x 1 nm	Broad, Peak at 808 nm
Graphene[12]	60 nm (diameter)	Broad, no specific peaks
Copper Sulfide NPs[14-16]	5 nm (diameter)	990 nm
Carbon Nanodots (CNDs)[13]	21 nm (diameter)	Broad, no specific peaks
CNDs in Organosilica[22]	1.5 nm in 100 nm	Broad, no specific peaks

As described in Chapter 3, a novel, controllable microwave synthesis for CuS nanodiscs has been developed. Additionally, particles with diameter close to the desired ~5.5 nm show the highest energy plasmon resonance, making these particles ideal for a potential application in photothermal therapy. While the plasmon resonance still occurs ~1175 nm, a lower energy than that of the 808 nm laser typically used to study photothermal effects, a simple solution presents itself. Rather than using a different size particle, it is quite possible and reasonable to use a different energy laser for these experiments, specifically 1064 nm. In previous literature, 1064 nm lasers have been used to study CuS nanoparticles in the context of a bioimaging technique, photoacoustic tomography (PAT).[30] PAT is a technique based on a similar process as PTT, the only difference being the amount of heat generated: in PAT the desire is as a diagnostic, not a therapeutic, where the generated heat is being detected. Specifically, only mK temperature increases are needed to generate a PAT signal,[31] while several degree K increases are need for PTT.[6] However, by using either higher concentrations of particles, higher intensity lasers, or increased exposure time, apoptosis can be induced. While the energy of 808 nm light is 1.53 eV, about 30% higher than 1064 nm light (1.16 eV), the absorption of CuS at 1064 nm is ~2-3 times higher than at 808 nm, so sufficient heating should be obtainable. This chapter focuses on studying the photothermal effect to verify this hypothesis, and it was found that these particles under the explored conditions do exhibit a photothermal effect.

Experimental

Transfer to Aqueous Solution and Characterization

The particles were synthesized as described in Chapter 3. However, as described in this chapter, the particles are hydrophobic due to their oleylamine coating. As particles for biological applications need to be dispersible in water, a ligand exchange was performed post-synthesis to increase hydrophilicity. Specifically, the procedure of Hofmann *et al*.[32] was adapted for use with CuS nanoparticles. After the synthesis, the particles were dispersed in toluene and 5 mL of this toluene dispersion was mixed with 1 mL of 10 mg/mL sodium dodecyl sulfate (SDS) in ethanol. The mixture was allowed to equilibrate for 1 hour, followed by rotary evaporation to remove both organic solvents. Finally, water was added and the solution was lightly bath sonicated to facilitate dispersion. Following dispersion, the particles were analyzed with UV-Vis-NIR spectroscopy and TEM.

Photothermal Effect Measurement

To study the PTE, a pulsed Nd:YAG laser (10 Hz, 5 ns pulse) was used to irradiate the sample. The main output wavelengths of this laser are 1064, 532 and 266 nm, so a long pass filter at 750 nm was inserted in the beam path to ensure that any heating effects arose only from the NIR (1064 nm) photons, and not the visible/UV. To hold the sample, a custom cuvette holder was designed and 3D printed. For the measurements, a sample was placed in the cuvette in the beam path and a thermocouple was inserted to monitor the temperature as a function of time. Specifically, temperature readings were taken at 1 min intervals over the course of 20 minutes. These experiments

were performed using a laser output of 350 mW and a spot size of ~5 mm, giving a power density on the sample of 1.8 W/cm^2. DI H_2O was also used as a control, to make sure that any observed heating is from the CuS NPs and not the solvent or thermocouple.

Results and Discussion

As described in Table 4.1, an ideal particle will have a small size and have a peak absorption near the chosen irradiation wavelength. Based on Table 3.1, the CuS NPs synthesized in a 5 minute reaction have the smallest diameter (6.5 nm), and absorption wavelength closest to 1064 nm (1176 nm). For this reason, these particles were chosen for transfer to aqueous solution and study in PTE measurements. To increase aqueous dispersibility a few capping agents (polyethylene glycol, citric acid, and mercaptopropanoic acid) had previously been tested, however only the above described transfer using SDS showed significant improvement in dispersibility. After performing the above steps, a green solution with minimal precipitate was obtained. It should be noted that within the span of a few days, the particles would begin aggregating and settling out of suspension, so this method still needs to be optimized for further studies. Additionally, this means that purification and preparation of solutions of known concentration was not able to be performed. Therefore, all of the characterizations and PTE measurements were performed within 24 hours off ligand exchange. In contrast, the originally synthesized CuS particles showed excellent stability when dispersed in non-polar organic solvents (toluene, chloroform, etc.).

Upon dispersal in water, TEM was performed (Fig. 4.1) to ensure that the particles were unaffected by the transfer. As can be seen in the TEM microgram, the

shape and small size of the NPs has been retained on transfer. Unlike in the previous TEM micrograms (Fig. 3.1), there is no preferred orientation for self-assembly of the particles. Instead, some of the particles are parallel to the support film and appear as circles or triangles, while others are perpendicular to the support film and appear as rods. No significant aggregation is observed, indicating that the transfer has been successful.

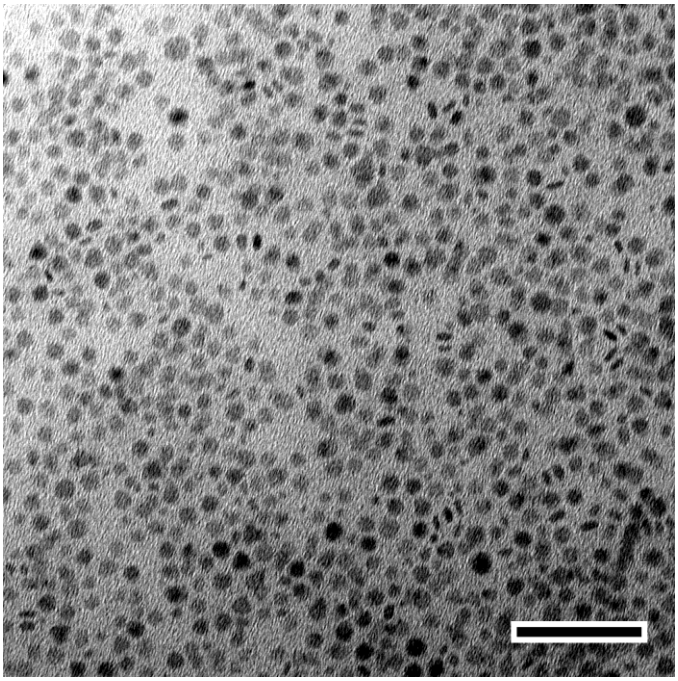

Figure 4.1. TEM of Water-Dispersed CuS. The scale bar on this image is 50 nm.

As the resonant frequency of a plasmon is dependent on the local dielectric constant around the particle (Eq. 3.1.), UV-Vis-NIR spectroscopy was performed on the particles in toluene (before addition of SDS) and in water (after addition of SDS) (Fig. 4.2). In these spectra it can be seen that the plasmon peak is slightly weaker and red-shifted in water, but the absorption at shorter wavelengths is enhanced. The weakening and shift of the plasmon may be the result of multiple factors. First is the change in

dielectric constant by the addition of SDS and transfer to water. There are multiple factors involved (dielectric constants of the capping agents and solvents) making exact prediction of the change in dielectric complicated, but it was expected that there would be a change. Additionally, there may be some formation of copper oxides, resulting in a loss of doping and therefore shifting the plasmon to lower energy. Regardless of the source of the change, the plasmon peak is still present, making it theoretically possible for these particles to exhibit a photothermal effect.

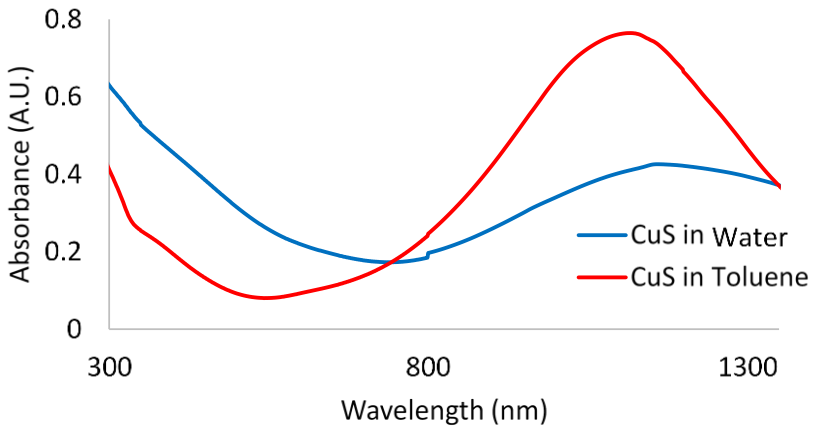

Figure 4.2. UV-Vis of Water-Dispersed CuS. UV-Vis-NIR of CuS NPs in toluene (red) and water (blue). Note that the discontinuity at 800 nm is due to the instrument changing detectors.

The photothermal effect measurements were carried out as described above. Due to the complications listed above, it is not possible to know the exact concentration of CuS in solution, however the synthetic steps suggest that the concentration is no greater than 0.5 mg/mL (~5.2 mM CuS). This solution was then irradiated with 1064 nm light as a function of time (Fig. 4.3). Over the course of treatment, the water control increased a

total of 2°C, a temperature change this is not expected to have any negative biological results. Conversely, during this same time period the CuS NPs heated from 24.1 to 38.2°C, an increase of 14.1°C. While a temperature of 38.2°C is not sufficient to cause damage, typical body temperature is significantly higher than ambient (37°C). A 14.1°C increase from normal body temperature would result in a temperature of 51.1°C, enough to cause rapid necrotic cell death.[6] As a further comparison, Li *et al*. found a temperature increase to ~37°C over 5 minutes, but the temperature then stabilized over that period.[15] While the temperature increase was comparable between their work and our own, their experiment used a lower concentration (0.77 mM), but a significantly higher laser output power (24 W/cm^2). Since there have not been studies on exactly how concentration and laser power correlate to heating, it is hard to directly compare these results. However, since absorption is linear in concentration and temperature increase is proportional to energy, it is expected that these results are at least comparable. Another interesting result is that the temperature increase over the first few minutes is significantly higher, raising 7.3°C in the first 5 minutes, enough to start inducing damage.

While these results combined together do suggest that this synthesis of CuS and a pulsed 1064 nm laser can both be used in potential photothermal applications, there are still a number of issues that need to be addressed. While some of these are in a more application-based issues, there are still a number of fundamental questions to be addressed as well. For implementation into photothermal therapy, issues of dispersion and targeting still need to be addressed to obtain an optimal treatment. From a more

fundamental perspective, the issues of heating mechanism and efficiency still need to be addressed.

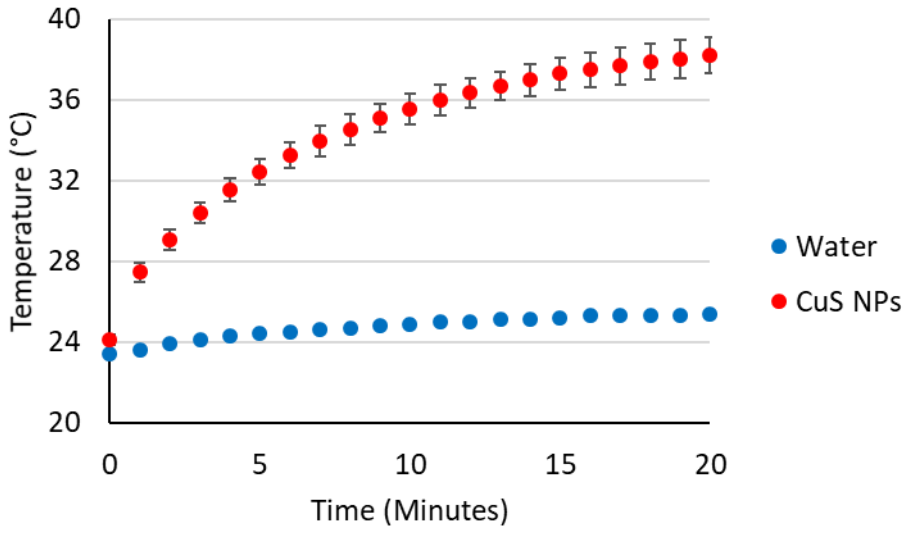

Figure 4.3. Laser Heating Curve of CuS. Laser heating curves for water (blue) and CuS NPs in water (Red). All experiments were conducted with a laser power of 1.8 W/cm^2, and the CuS data represents the average and standard deviation of 3 measurements.

One of the issues with understanding the heating mechanism is that it does vary between different classes of particles. When relaxation happens for excited electrons in a semiconducting or molecular material with well-defined bands or quantized states, this relaxation is accompanied by either radiative (photon) or non-radiative (heat) energy emission.[6] However, the process of plasmon relaxation is still an active field of research, with most of the studies being focused on traditional noble metal plasmons (Au, Ag, Pt),[33-35] making it difficult to apply to asymmetrical materials like CuS. Understanding of the heating mechanism is further complicated by the presence of capping agents that must transfer the heat from the NPs to the bulk media.

Based on a number of different parameters, the efficiency of the process can be estimated. A number of potential error sources exist, so this value may not be entirely accurate. As can be seen in Fig. 4.3, the temperature increase as a function of time is non-linear. The main cause of this is likely thermal transfer to parts of the solution that are not actively being irradiated. The design of the setup was such that only a ~5 mm spot near the top of the cuvette was actively being treated, while the remainder of the sample was not. For the measurements, the thermocouple was placed in the vicinity of the laser spot, to give the most accurate reading. In estimating the efficiency, the total energy required for a given temperature increase can simply be calculated using heat capacity and the mass of water being treated. The volume of the cuvette that was being irradiated was ~0.2 mL, and therefore ~0.2 g of water was used in the calculation. The incident energy can be calculated simply as the laser power output (0.35 W) multiplied by the irradiation time. Dividing the required energy by the incident energy can give the overall efficiency over time (Fig. 4.4). As can be seen in the figure, the efficiency of the first step is 13.4%, but drops with longer time due to thermal dissipation. While absorption efficiencies for gold NPs of close to 100% have been reported,[36] the efficiency of CuS in PTT has not been reported.

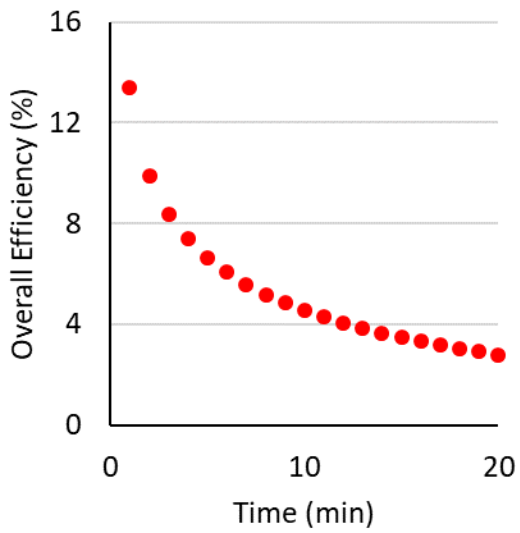

Figure 4.4. Photothermal Efficiency. Efficiency of laser to thermal heat conversion as a function of sample irradiation time. Efficiency was calculated based on laser power and the heat capacity of water.

Conclusion

In conclusion, these experiments have provided proof-of-concept for the use of a pulsed 1064 nm laser and microwave-synthesized CuS NPs in photothermal therapy. Specifically, hydrophobic CuS NPs were successfully transferred to aqueous phase using SDS as a capping agent. TEM was performed to show that the morphology of the particles was not significantly altered by this reaction, and UV-Vis-NIR was performed to examine the plasmon peak. Finally, the particles were treated with NIR light and a significant temperature increase (14.1°C) vs. DI water control (2°C) was observed. These results show that this methodology has potential for use in biological systems, starting with *in vitro* studies.

References

1. National Cancer Institute https://www.cancer.gov/about-cancer/understanding/statistics. **2017**.

2. Jemal, A.; Ward, E. M.; Johnson, C. J.; Cronin, K. A.; Ma, J.; Ryerson, B.; Mariotto, A.; Lake, A. J.; Wilson, R.; Sherman, R. L.; Anderson, R. N.; Henley, S. J.; Kohler, B. A.; Penberthy, L.; Feuer, E. J.; Weir, H. K., Annual Report to the Nation on the Status of Cancer, 1975-2014, Featuring Survival. *J Natl Cancer Inst* **2017,** *109* (9).

3. Zwicke, G. L.; Mansoori, G. A.; Jeffery, C. J., Utilizing the folate receptor for active targeting of cancer nanotherapeutics. *Nano Rev* **2012,** *3*.

4. Urruticoechea, A.; Alemany, R.; Balart, J.; Villanueva, A.; Vinals, F.; Capella, G., Recent Advances in Cancer Therapy: An Overview. *Current Pharmaceutical Design* **2010,** *16*, 3-10.

5. Hildebrandt, B.; Wust, P.; Ahlers, O.; Dieing, A.; Sreenivasa, G.; Kerner, T.; Felix, R.; Riess, H., The cellular and molecular basis of hyperthermia. *Critical Reviews in Onocology/Hematology* **2002,** *43*, 33-56.

6. Jaque, D.; Martinez Maestro, L.; del Rosal, B.; Haro-Gonzalez, P.; Benayas, A.; Plaza, J. L.; Martin Rodriguez, E.; Garcia Sole, J., Nanoparticles for photothermal therapies. *Nanoscale* **2014,** *6* (16), 9494-530.

7. Hirsch, L. R.; Stafford, R. J.; Bankson, J. A.; Sershen, S. R.; Rivera, B.; Price, R. E.; Hazle, J. D.; Halas, N. J.; West, J. L., Nanoshell-mediated near-infrared thermal therapy of tumors under magnetic resonance guidance. *Proc Natl Acad Sci U S A* **2003,** *100* (23), 13549-54.

8. Huang, X.; El-Sayed, I. H.; Qian, W.; El-Sayed, M. A., Cancer cell imaging and photothermal therapy in the near-infrared region by using gold nanorods. *J Am Chem Soc* **2006,** *128* (6), 2115-20.

9. Huang, X.; Jain, P. K.; El-Sayed, I. H.; El-Sayed, M. A., Plasmonic photothermal therapy (PPTT) using gold nanoparticles. *Lasers Med Sci* **2008,** *23* (3), 217-28.

10. Lu, W.; Singh, A. K.; Khan, S. A.; Senapati, D.; Yu, H.; Ray, P. C., Gold nano-popcorn-based targeted diagnosis, nanotherapy treatment, and in situ monitoring of photothermal therapy response of prostate cancer cells using surface-enhanced Raman spectroscopy. *J Am Chem Soc* **2010,** *132* (51), 18103-14.

11. Kam, N. W.; O'Connell, M.; Wisdom, J. A.; Dai, H., Carbon nanotubes as multifunctional biological transporters and near-infrared agents for selective cancer cell destruction. *Proc Natl Acad Sci U S A* **2005,** *102* (33), 11600-5.

12. Yang, K.; Zhang, S.; Zhang, G.; Sun, X.; Lee, S. T.; Liu, Z., Graphene in mice: ultrahigh in vivo tumor uptake and efficient photothermal therapy. *Nano Lett* **2010,** *10* (9), 3318-23.

13. Li, Y.; Zhang, X.; Zheng, M.; Liu, S.; Xie, Z., Dopamine carbon nanodots as effective photothermal agents for cancer therapy. *RSC Adv.* **2016,** *6* (59), 54087-54091.

14. Zhou, M.; Zhang, R.; Huang, M.; Lu, W.; Song, S.; Melancon, M. P.; Tian, M.; Liang, D.; Li, C., A Chelator-Free Multifunctional (^{64}Cu)CuS Nanoparticle Platform for Simultaneous Micro-PET-CT Imaging and Photothermal Ablation Therapy. *J Am Chem Soc* **2010,** *132*, 15351-15358.

15. Li, Y.; Lu, W.; Huang, Q.; Huang, M.; Li, C.; Chen, W., Copper sulfide nanoparticles for photothermal ablation of tumor cells. *Nanomedicine* **2010,** *5* (8), 1161-1181.

16. Zhou, M.; Li, J.; Liang, S.; Sood, A. K.; Liang, D.; Li, C., CuS Nanodots with Ultrahigh Efficient Renal Clearance for Positron Emission Tomography Imaging and Image-Guided Photothermal Therapy. *ACS Nano* **2015,** *9* (7), 7085-96.

17. Wang, X.; Wang, C.; Cheng, L.; Lee, S. T.; Liu, Z., Noble metal coated single-walled carbon nanotubes for applications in surface enhanced Raman scattering imaging and photothermal therapy. *J Am Chem Soc* **2012,** *134* (17), 7414-22.

18. Zhong, Y.; Wang, C.; Cheng, R.; Cheng, L.; Meng, F.; Liu, Z.; Zhong, Z., cRGD-directed, NIR-responsive and robust AuNR/PEG-PCL hybrid nanoparticles for targeted chemotherapy of glioblastoma in vivo. *J Control Release* **2014,** *195*, 63-71.

19. Li, J.; Hu, Y.; Yang, J.; Wei, P.; Sun, W.; Shen, M.; Zhang, G.; Shi, X., Hyaluronic acid-modified Fe3O4@Au core/shell nanostars for multimodal imaging and photothermal therapy of tumors. *Biomaterials* **2015,** *38*, 10-21.

20. Li, J.; Lyv, Z.; Li, Y.; Liu, H.; Wang, J.; Zhan, W.; Chen, H.; Chen, H.; Li, X., A theranostic prodrug delivery system based on Pt(IV) conjugated nano-graphene oxide with synergistic effect to enhance the therapeutic efficacy of Pt drug. *Biomaterials* **2015,** *51*, 12-21.

21. Noh, M. S.; Lee, S.; Kang, H.; Yang, J. K.; Lee, H.; Hwang, D.; Lee, J. W.; Jeong, S.; Jang, Y.; Jun, B. H.; Jeong, D. H.; Kim, S. K.; Lee, Y. S.; Cho, M. H., Target-specific near-IR induced drug release and photothermal therapy with accumulated Au/Ag hollow nanoshells on pulmonary cancer cell membranes. *Biomaterials* **2015,** *45*, 81-92.

22. Singh, R. K.; Patel, K. D.; Mahapatra, C.; Kang, M. S.; Kim, H.-W., C-Dot Generated Bioactive Organosilica Nanospheres in Theranostics: Multicolor Luminescent and Photothermal Properties Combined with Drug Delivery Capacity. *ACS Applied Materials & Interfaces* **2016,** *8* (37), 24433-24444.

23. Cheng, L.; Gong, H.; Zhu, W.; Liu, J.; Wang, X.; Liu, G.; Liu, Z., PEGylated Prussian blue nanocubes as a theranostic agent for simultaneous cancer imaging and photothermal therapy. *Biomaterials* **2014,** *35* (37), 9844-52.

24. Li, W.; Rong, P.; Yang, K.; Huang, P.; Sun, K.; Chen, X., Semimetal nanomaterials of antimony as highly efficient agent for photoacoustic imaging and photothermal therapy. *Biomaterials* **2015,** *45*, 18-26.

25. Liu, T.; Shi, S.; Liang, C.; Shen, S.; Cheng, L.; Wang, C.; Song, X.; Goel, S.; Barnhart, T. E.; Cai, W.; Liu, Z., Iron oxide decorated MoS2 nanosheets with double PEGylation for chelator-free radiolabeling and multimodal imaging guided photothermal therapy. *ACS Nano* **2015,** *9* (1), 950-60.

26. Yang, K.; Yang, G.; Chen, L.; Cheng, L.; Wang, L.; Ge, C.; Liu, Z., FeS nanoplates as a multifunctional nano-theranostic for magnetic resonance imaging guided photothermal therapy. *Biomaterials* **2015,** *38*, 1-9.

27. Liu, J.; Wang, P.; Zhang, X.; Wang, L.; Wang, D.; Gu, Z.; Tang, J.; Guo, M.; Cao, M.; Zhou, H.; Liu, Y.; Chen, C., Rapid Degradation and High Renal Clearance of Cu3BiS3 Nanodots for Efficient Cancer Diagnosis and Photothermal Therapy in Vivo. *ACS Nano* **2016,** *10* (4), 4587-98.

28. Henderson, T. A.; Morries, L. D., Near-infrared photonic energy penetration: can infrared phototherapy effectively reach the human brain? *Neuropsychiatr Dis Treat* **2015,** *11*, 2191-208.

29. Choi, H. S.; Liu, W.; Misra, P.; Tanaka, E.; Zimmer, J. P.; Itty Ipe, B.; Bawendi, M. G.; Frangioni, J. V., Renal clearance of quantum dots. *Nat Biotechnol* **2007,** *25* (10), 1165-70.

30. Ku, G.; Zhou, M.; Song, S.; Huang, Q.; Hazle, J.; Li, C., Copper Sulfide Nanoparticles As a New Class of Photoacoustic Contrast Agent for Deep Tissue Imaging at 1064 nm. *ACS Nano* **2012,** *6* (8), 7489-6496.

31. Xia, J.; Yan, J.; Wang, L. V., Photoacoustic tomography: principles and advances. *Progress In Electromagnetics Research* **2014,** *147*, 1-22.

32. Hofmann, D. M.; Fairbrother, D. H.; Hamers, R. J.; Murphy, C. J., Two-Phase Synthesis of Gold–Copper Bimetallic Nanoparticles of Tunable Composition: Toward

Optimized Catalytic CO2 Reduction. *ACS Applied Nano Materials* **2019,** *2* (6), 3989-3998.

33. Besteiro, L. V.; Kong, X.-T.; Wang, Z.; Hartland, G.; Govorov, A. O., Understanding Hot-Electron Generation and Plasmon Relaxation in Metal Nanocrystals: Quantum and Classical Mechanisms. *ACS Photonics* **2017,** *4* (11), 2759-2781.

34. Kamarudheen, R.; Castellanos, G. W.; Kamp, L. P. J.; Clercx, H. J. H.; Baldi, A., Quantifying Photothermal and Hot Charge Carrier Effects in Plasmon-Driven Nanoparticle Syntheses. *ACS Nano* **2018,** *12* (8), 8447-8455.

35. Wang, Q.; Wang, H.; Yang, Y.; Jin, L.; Liu, Y.; Wang, Y.; Yan, X.; Xu, J.; Gao, R.; Lei, P.; Zhu, J.; Wang, Y.; Song, S.; Zhang, H., Plasmonic Pt Superstructures with Boosted Near-Infrared Absorption and Photothermal Conversion Efficiency in the Second Biowindow for Cancer Therapy. *Advanced Materials* **2019,** *31* (46), 1904836.

36. Maestro, L. M.; Haro-González, P.; Coello, J. G.; Jaque, D., Absorption efficiency of gold nanorods determined by quantum dot fluorescence thermometry. *Applied Physics Letters* **2012,** *100* (20), 201110.

CHAPTER V

CONCLUSIONS AND FUTURE WORK

The primary goal of this work was to explore the properties of emerging nanomaterials, in order to help implementation into potential future applications. As the studied materials are poorly understood from an experimental perspective, it was important to use both experimental and computational methods to explore the interesting optical properties. Specifically, the chosen computational method was density functional theory (DFT), a computational technique that allows for reasonable calculation times when studying the quantum mechanical properties of complicated systems. However, while the use of DFT was shared for both studied materials, the implementation was dependent on the chemical nature of the particle, i.e. either a molecular or periodic crystalline structure. In the case of molecular systems, a time-dependent DFT (TDDFT) approach was required to look at the transitions between quantized states. On the other hand, crystalline materials were studied by a novel analysis of traditional solid state properties; band structures and density of states.

Chapter II focused on the first of the studied materials, carbon nanodots (CNDs). Specifically, two different experimental syntheses were explored and each generated CNDs that have different optical properties, both in terms of absorption and emission. In order to help explain the observed differences, a number of different proposed structures were studied by TDDFT. The main result of these calculations was how the deformation

in the structure of the CND can affect the optical properties. Specifically, increased deformation resulted in more allowed optical transitions, but a general lessening of the absorption intensity. Further, as these deformations can affect the interlayer spacing of the graphitic structure, this result can help explain the difference in fluorescence intensity owing to the formation of trap states. Our group continues to use CNDs in many experimental studies for future applications, but there still remains more computational work that can be pursued. For example, additional structures can be studied by adding new elements, such as sulfur, changing the size of the graphitic sheet, or using multiple graphitic layers.

Chapter III focused on the second of the two studied materials, copper sulfide nanoparticles. For this work, a novel microwave synthesis was implemented allowing for size and plasmon control of the synthesized nanodiscs. Using the experimental results, charge carrier densities were calculated for each size of particle, initially in the range of 1.2-1.4 x 10^{22} cm^{-3}. However, one of the important factors in this calculation was the effective mass of the charge carriers and upon review of the literature it was found that this value had never been calculated for this material. Further, a theoretical charge carrier density was desired as a comparison to the experimental results. DFT calculations were used to obtain these values from the band structure and density of states, respectively. These calculations resulted in a theoretical effective mass of 0.3m_e and a charge carrier density of 9.8 x 10^{21} cm^{-3}. Using this new effective mass, the experimental charge carrier densities were recalculated as 4.7 – 5.3 x 10^{21} cm^{-3}, approximately half of the calculated value. There are still further experiments that can be conducted on this system, both in

terms of applications and synthesis. Currently, other students are working on using the plasmon in two different applications; as a sensor by coupling to gold nanoslits, and for photocatalysis. Additionally, the synthesis can be further explored by potentially changing the concentration to change morphology or by including other chalcogenides (selenium, tellurium) to adjust the electronic properties.

Chapter IV explored a potential application in photothermal therapy for the copper sulfide particles synthesized in Chapter III. The as-synthesized CuS particles were first transferred to water using SDS as a surfactant. TEM and UV-Vis-NIR were used to characterize particles after transfer. Photothermal measurements showed a significant temperature increase vs. control, and the overall efficiency of the process was calculated at each timestep. Combining these results suggest that these particles and laser setup can be used for a potential biological application. Before this application can be realized, additional tests and characterizations are needed. One area that needs improvement is on the aqueous stability; while SDS has significantly improved stability, the particles do settle over time. Determining the cytotoxicity of these particles is also paramount, to ensure that the particles themselves do not cause any damage to health tissues. Further, while the results of these experiments and other literature suggest that this treatment should induce apoptosis *in vitro* and *in vivo*, this needs to be confirmed. Finally, characterizing the particles both pre- and post-photothermal treatment may be useful as degradation of the particles could introduce unintentional side effects.

APPENDIX A

EXPERIMENTAL AND TIME-DEPENDENT DENSITY FUNCTIONAL THEORY MODELING STUDIES ON THE OPTICAL PROPERTIES OF CARBON NANODOTS

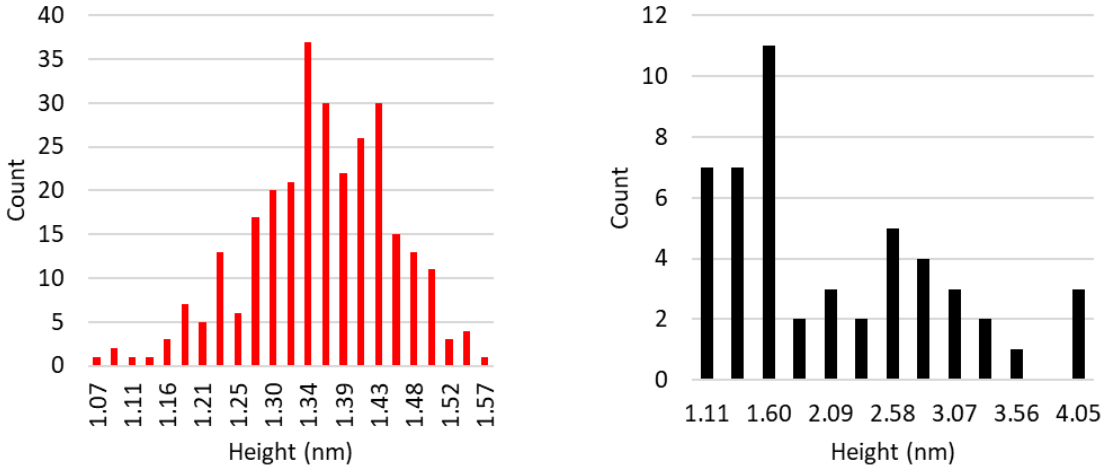

Figure A.S1. AFM Height Distributions for CNDs. AFM height distributions from Fig. 1 showing the size of suc-CNDs (red, left) and E-CNDs (black, right). These data show average sizes of 1.4 and 2.1 nm for suc-CNDs and E-CNDs, respectively.

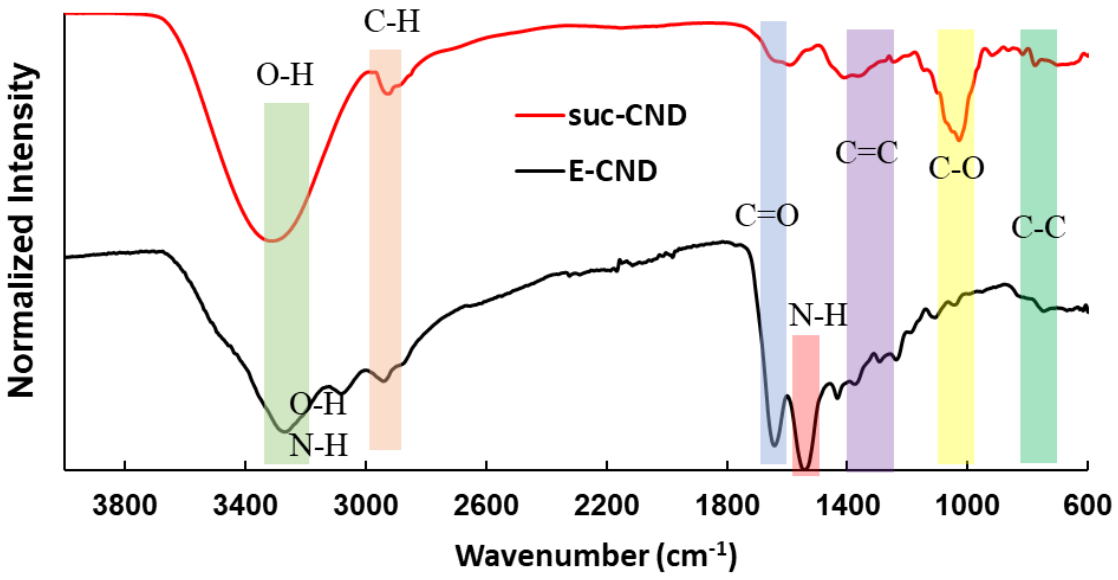

Figure A.S2. FTIR of CNDs. FTIR spectra for suc- (red) and E-CNDs (black). The spectra have been normalized and offset for clarity.

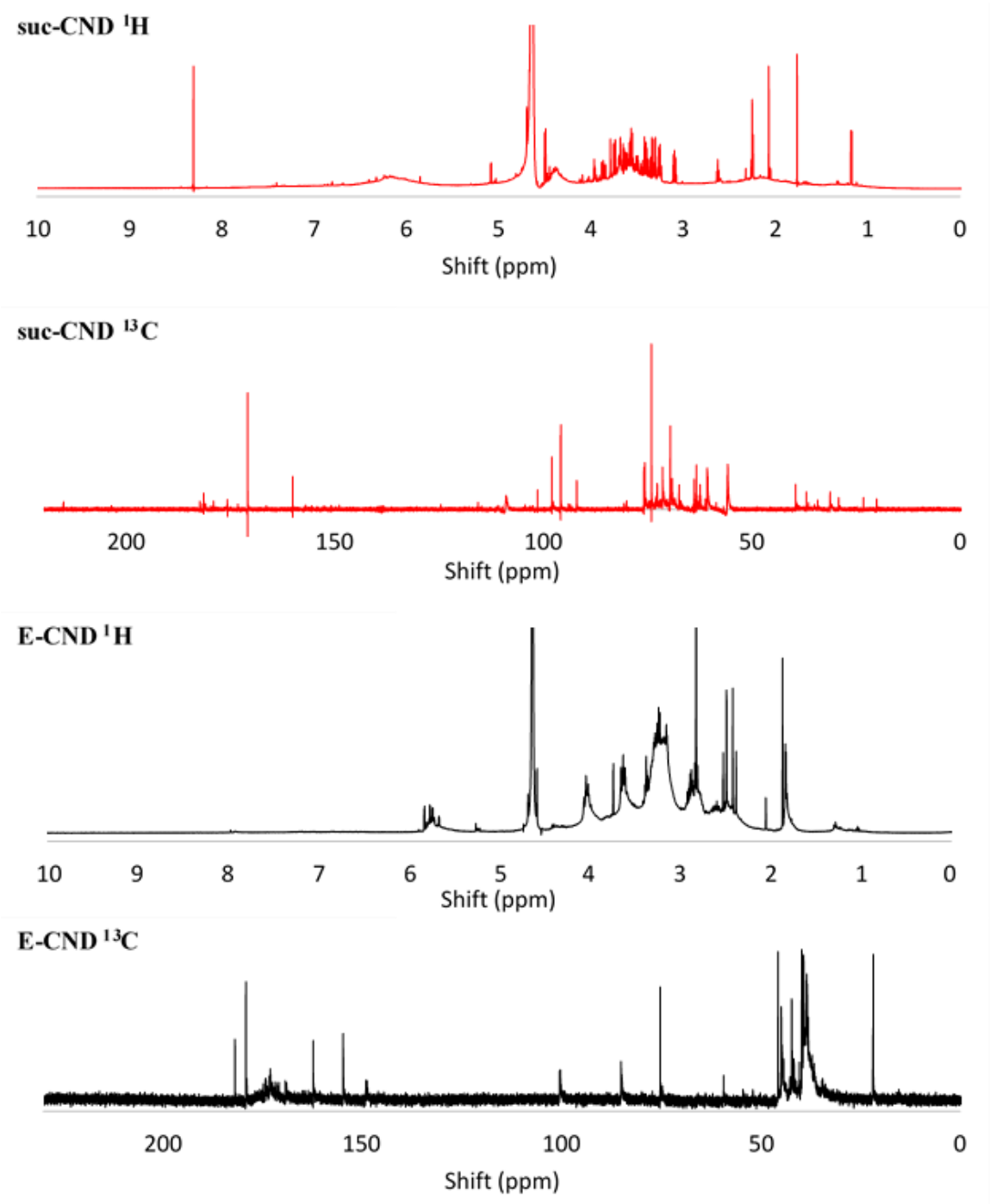

Figure A.S3. NMR of CNDs. ^{1}H and ^{13}C NMR of suc- (red) and E-CNDs (black). Each ^{1}H spectrum is the average of 64 scans, while the ^{13}C are the average of 100,000 scans. The suc-CND NMR was obtained with a 700 MHz NMR, while the E-CND NMR had to be obtained on a 400 MHz NMR, due to instrument failure.

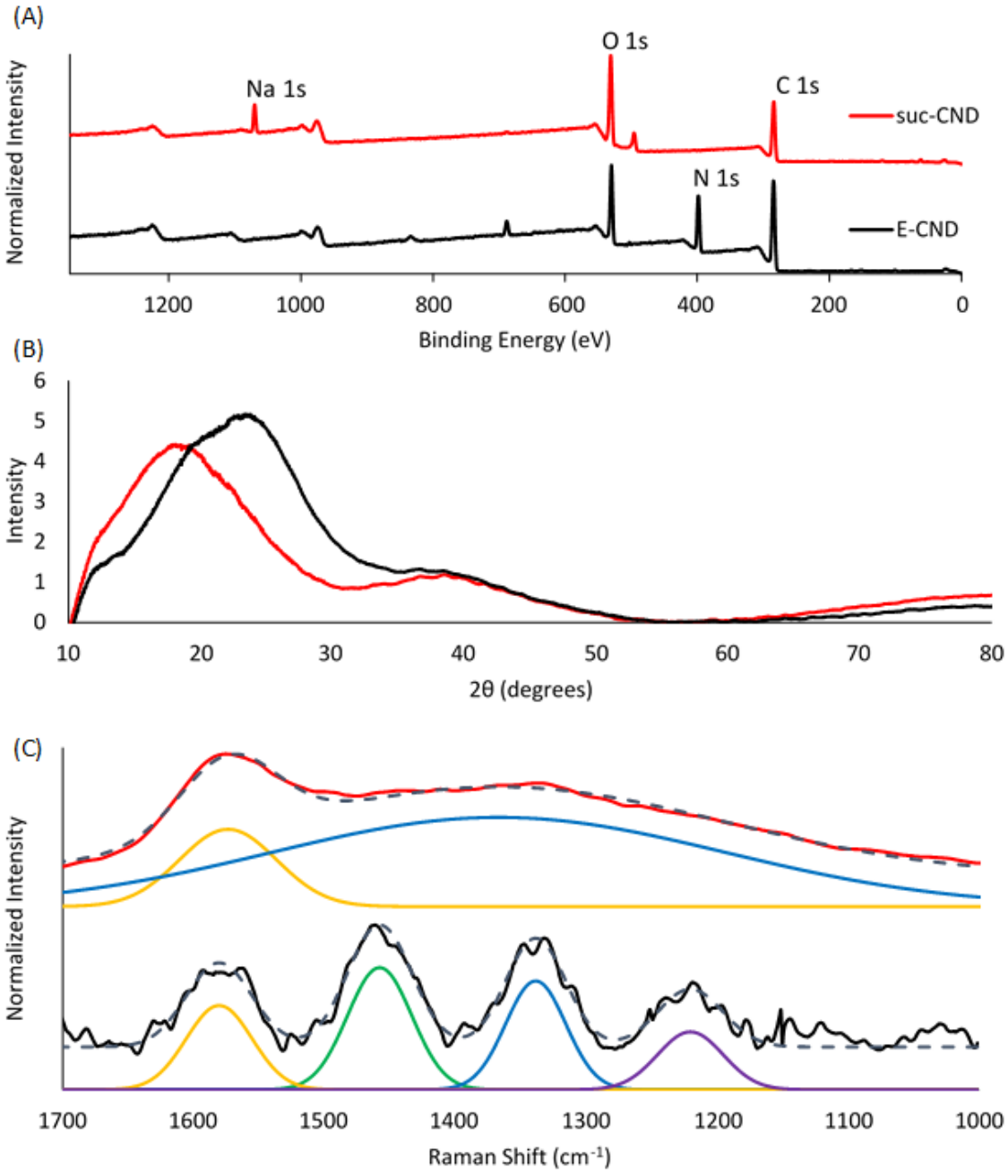

Figure A.S4. XPS, XRD, and Raman of CNDs. XPS (A), XRD (B), and Raman (C) of suc-CNDs (Red) and E-CNDs (Black). XPS have been offset for clarity, and the major elements identified. Raman have been offset for clarity, and peak deconvolution has been performed to isolate the G band (orange, ~1580 cm-1) and D band (blue, 1380 and 1366 cm-1 for suc-CND and E-CND respectively). The dashed gray line shows the peak fitting for each spectrum.

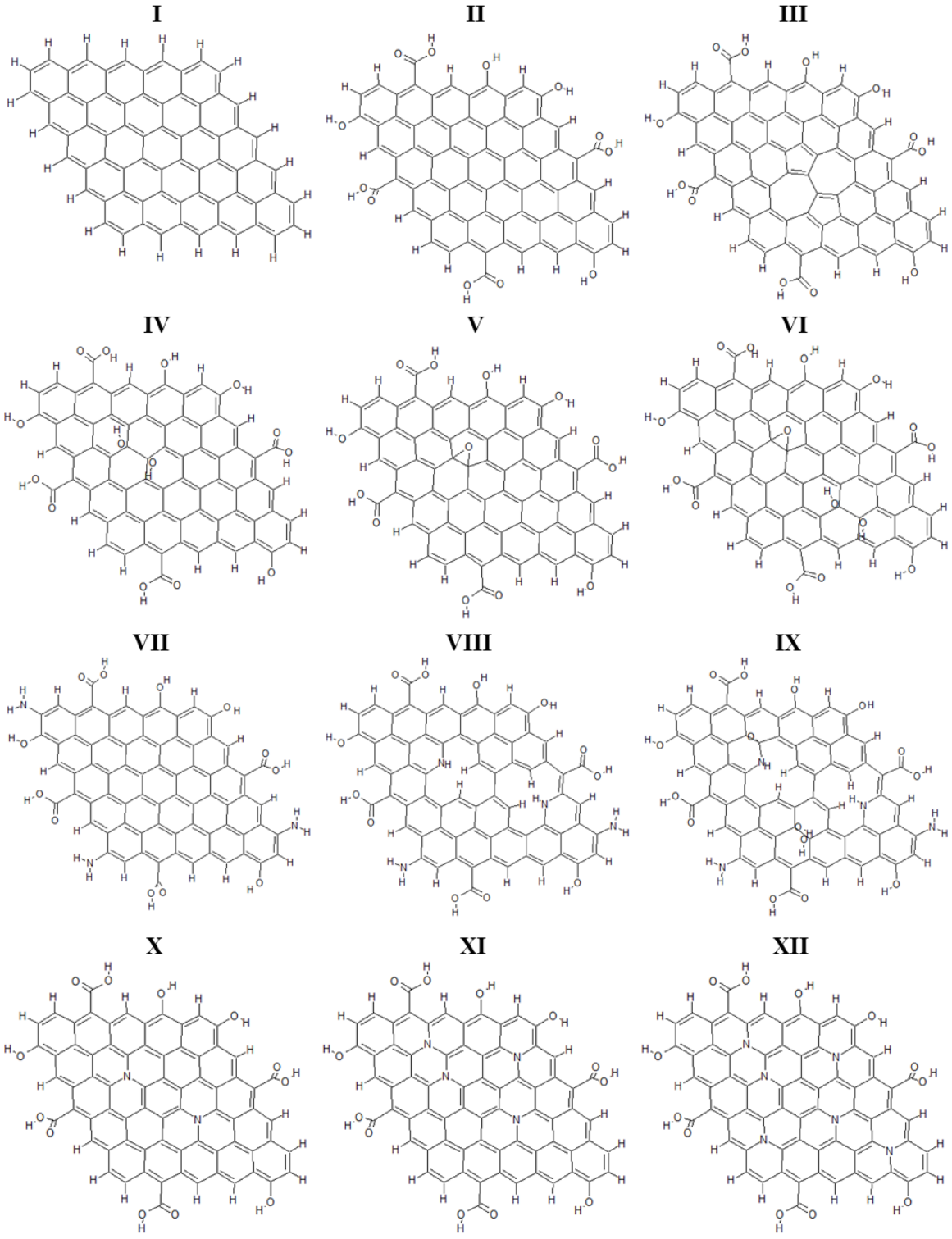

Figure A.S5. Studied CND Structures. Structures **I-XII** used in DFT calculations

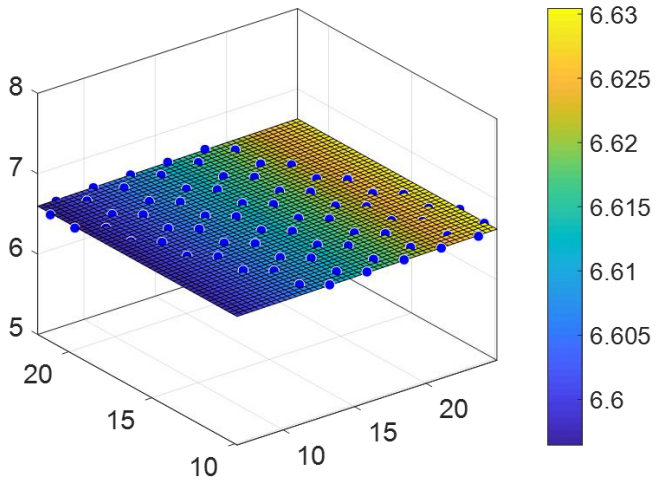

Figure A.S6. Representative Planar Fit of CNDs. Representative planar fitting using structure **I**.

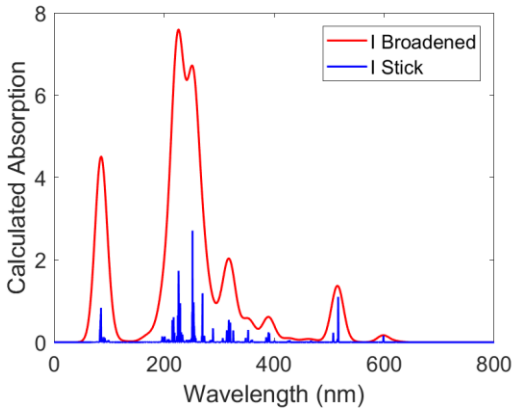
I Broadened
I Stick
Calculated Absorption
Wavelength (nm)
0
2
4
6
8
0
200
400
600
800

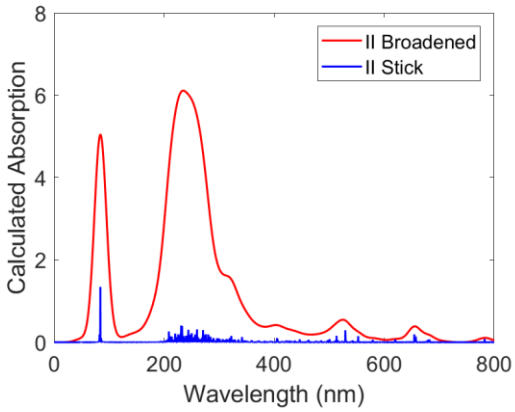
II Broadened
II Stick
Calculated Absorption
Wavelength (nm)
0
2
4
6
8
0
200
400
600
800

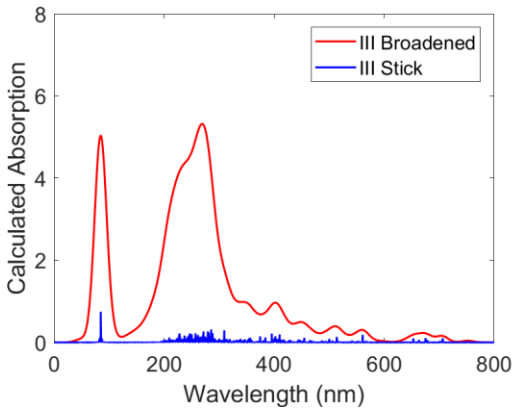
III Broadened
III Stick
Calculated Absorption
Wavelength (nm)
0
2
4
6
8
0
200
400
600
800

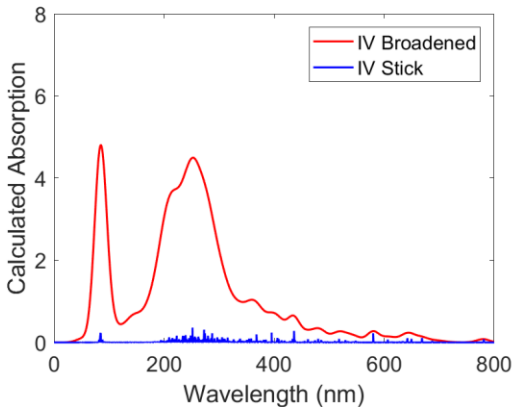
IV Broadened
IV Stick
Calculated Absorption
Wavelength (nm)
0
2
4
6
8
0
200
400
600
800

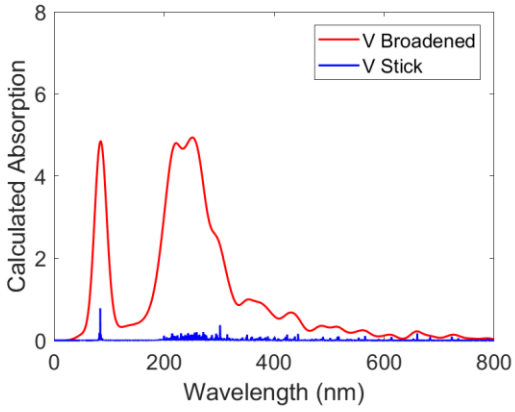
V Broadened
V Stick
Calculated Absorption
Wavelength (nm)
0
2
4
6
8
0
200
400
600
800

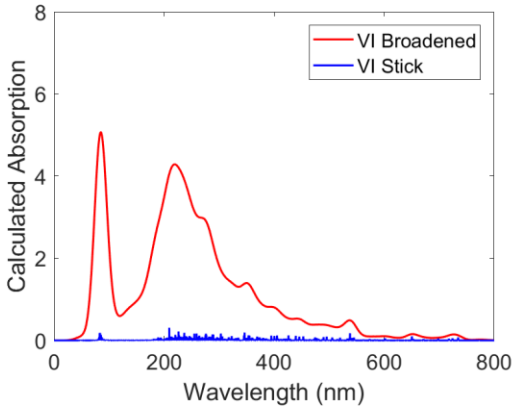
VI Broadened
VI Stick
Calculated Absorption
Wavelength (nm)
0
2
4
6
8
0
200
400
600
800

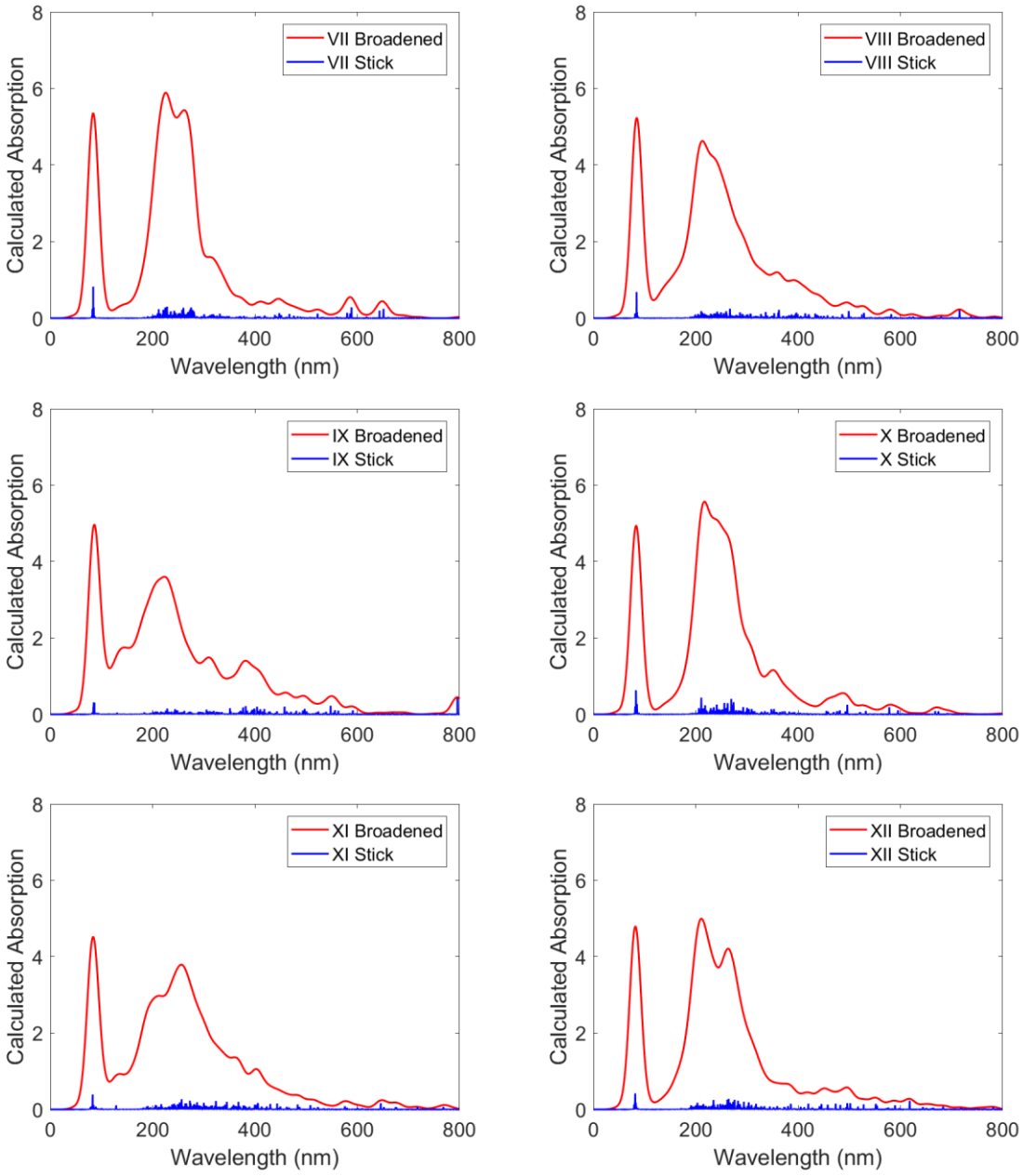

Figure A.S7 (Two pages). All Predicted UV-Vis CND Spectra. Gaussian broadened (red) and stick (blue) spectra from structures **I-XII**

APPENDIX B

NOVEL MICROWAVE SYNTHESIS OF NEAR-METALLIC COPPER SULFIDE NANODISCS WITH SIZE CONTROL: EXPERIMENTAL AND DFT STUDIES OF CHARGE CARRIER DENSITY

Table B.S1. Summary of Cu_xS Synthetic Methods

Author	Stoichiometry	Method	Preparation of Precursor(s)?	Reaction Time	Reaction Temp (°C)
Hsu *et al.* [1]	$Cu_{1.94}S$	Powder thermolysis	Yes	15-420 min	190-200
Luther *et al.* [2]	$Cu_{1.94}S$	Hot injection	Yes	3-12 min	180
Lee *et al.* [3]	Cu_2S	Solvothermal	No	1-20 min	190
Xie *et al.* [4]	CuS	Hot injection	Yes	10 min	180
Tang *et al.* [5]	Cu_2S	Solvothermal	No	10-60 min	200
Wang *et al.* [6]	$Cu_{1.42}S$	Hot injection	Yes	30 min	145
Hsu *et al.* [7]	$Cu_{1.96}S$	Powder thermolysis	Yes	Not given	200
	$Cu_{1.8}S$, CuS	Solvothermal	No	Not given	180
Kim *et al.* [8]	CuS	Solvothermal	Yes	30s	150
	CuS	Microwave	Yes	30 s	130
M. Liu *et al.* [9]	CuS	Repeated injections	Yes	7.5-22.5 min	RT
L. Liu *et al.* [10]	$Cu_{1.8}S$	Hot injection	Yes	5-15 min	180
	CuS	Phase transformation from $Cu_{1.8}S$	Yes ($Cu_{1.8}S$ Above)	1-5 days	RT
Xie *et al.* [11]	$Cu_{1.1}S$	Solvothermal	Yes	90 min	200
Ding *et al.* [12]	CuS	Hydrothermal	No	17 hr	90
Zhou *et al.* [13]	CuS	Hydrothermal	No	20 min	90
Thongtem *et al.* [14]	CuS	Microwave	No	20 min	
Ku *et al.* [15]	CuS	Hydrothermal	No	20 min	90
Y. Li *et al.* [16]	CuS	Hydrothermal	No	2 hr	50
Ni *et al.* [17]	CuS	Microwave	No	20 min	
H. Li *et al.* [18]	CuS	Microwave	No	30 min	

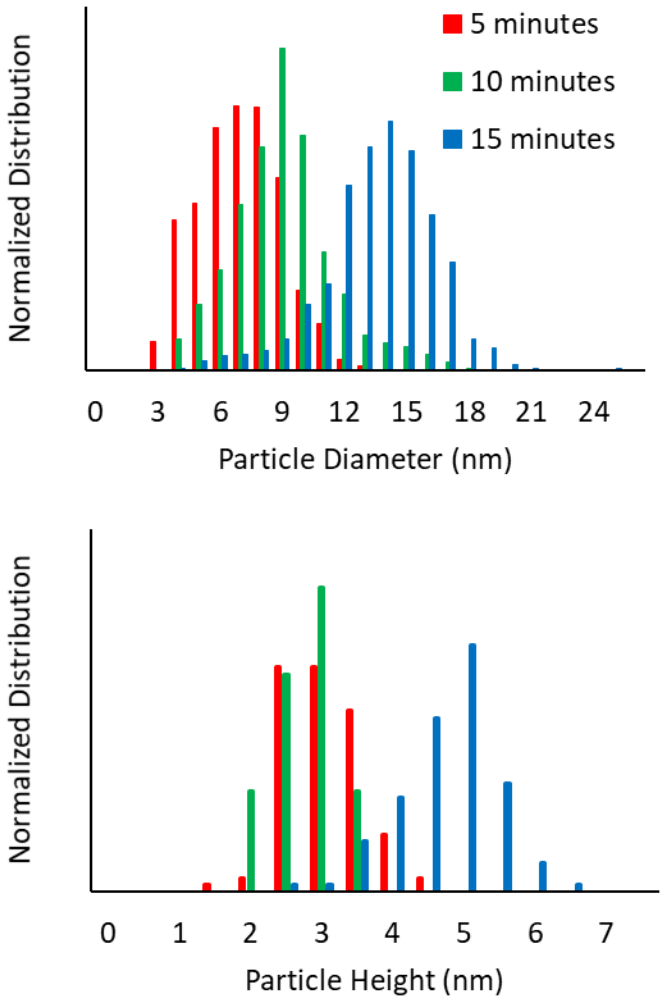

Figure B.S1. TEM Size Distributions for CuS. Normalized distributions for the diameter (top) and height (bottom) of the synthesized CuS NPs. The diameter distributions come from several hundred particles, while each height distribution comes from 100 particles. The insets on the micrographs show the electron diffraction pattern, and the scale bar on all images is 100 nm.

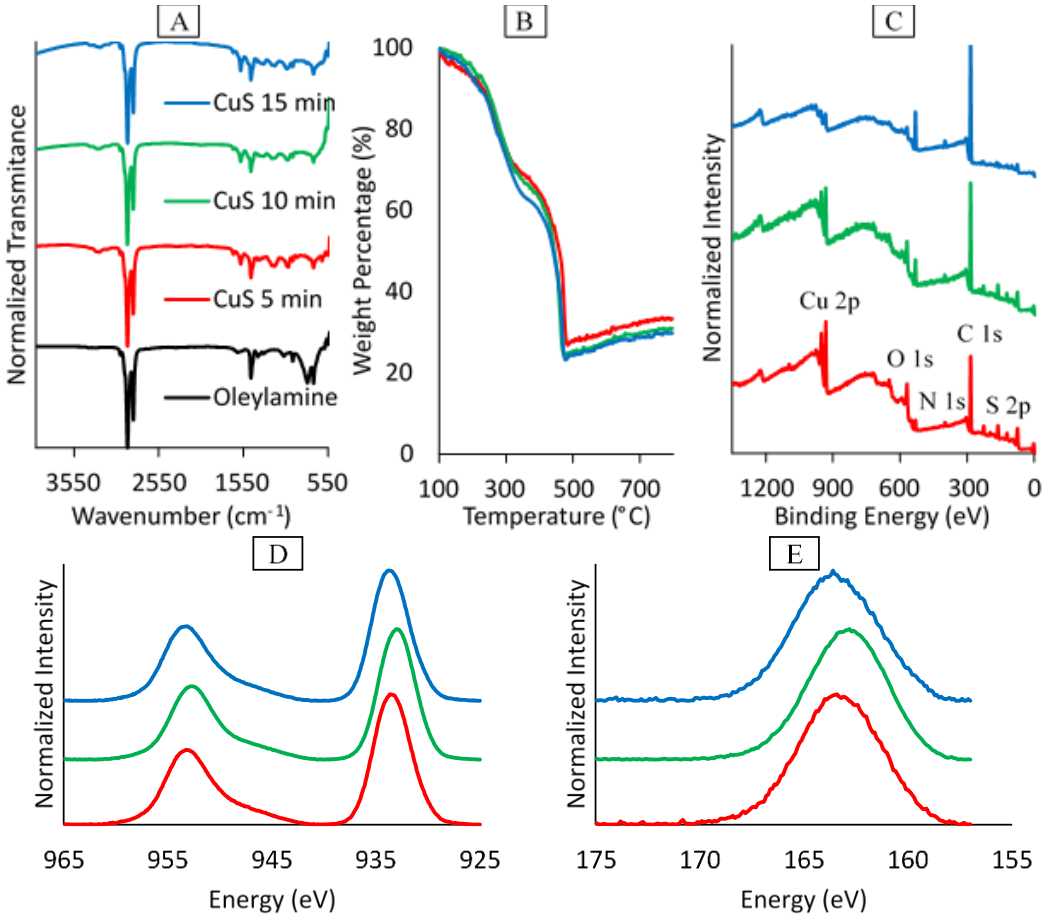

Figure B.S2. FTIR, TGA, and XPS for CuS NPs. FTIR (A), TGA (B), and XPS (C-E) for CuS NPs synthesized for 5 (red), 10 (green), or 15 (blue) minutes. The additional black curve in the FTIR is that of pure oleylamine. The TGA experiments were performed under a N_2 atmosphere to prevent oxidation. In the XPS survey plot (C), the major elements are labeled with their corresponding peaks. The copper and sulfur L-edges are given in (D) and (E), respectively.

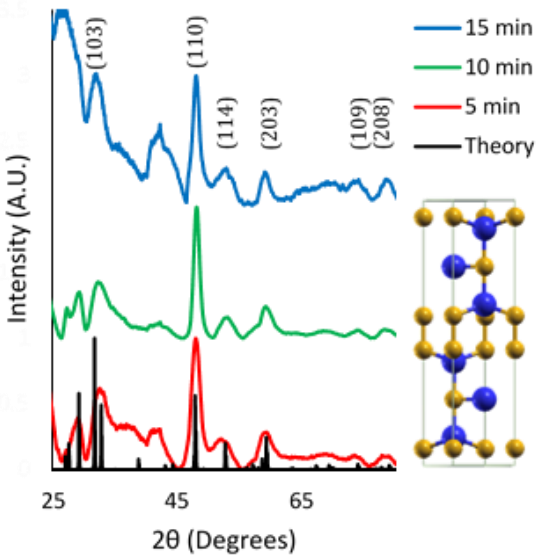

Figure B.S3. XRD for CuS NPs. Experimental and predicted XRD data for CuS. Data is shown for CuS NPs synthesized for 5 (red), 10 (green), or 15 (blue) minutes, plus a predicted pattern (black). The major peaks are labeled, and the inset shows the structure used for predictions.

Table B.S2. Elemental Analysis from XPS

Sample	**% Cu**	**% S**
5 min	8.56	8.03
10 min	5.40	5.43
15 min	1.78	2.15

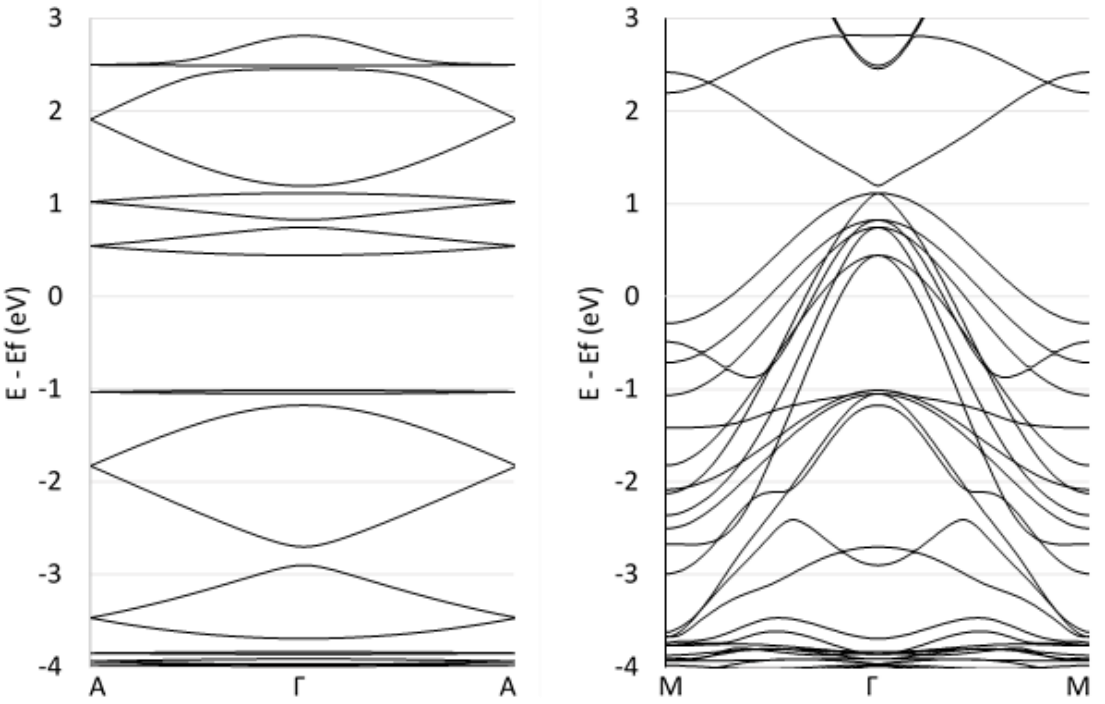

Figure B.S4. Additional CuS Band Structures. Calculated band structures for CuS in the Γ-A direction (left) and the Γ-M direction (right). The band structures show a traditional semiconducting band structure with a bandgap of 1.45 eV in the Γ-A direction (along the c-axis), and a more metallic band structure in the Γ-M direction (within the XY plane). The left figure was used to calculate the transversal effective mass at the Γ point, while the right figure was used to calculate the lateral effective mass around the Fermi energy.

References

1. Hsu, S.-W.; Bryks, W.; Tao, A. R., Effects of Carrier Density and Shape on the Localized Surface Plasmon Resonances of Cu2–xS Nanodisks. Chemistry of Materials 2012, 24 (19), 3765-3771.

2. Luther, J. M.; Jain, P. K.; Ewers, T.; Alivisatos, A. P., Localized surface plasmon resonances arising from free carriers in doped quantum dots. Nat Mater 2011, 10 (5), 361-6.

3. Lee, H.; Yoon, S. W.; Kim, E. J.; Park, J., In-Situ Growth of Copper Sulfide Nanocrystals on Multiwalled Carbon Nanotubes and Their Application as Novel Solar Cell and Amperometric Glucose Sensor Materials. Nano Lett 2007, 7 (3), 778-784.

4. Xie, Y.; Carbone, L.; Nobile, C.; Grillo, V.; D'Agostino, S.; Sala, F. D.; Giannini, C.; Altamura, D.; Oelsner, C.; Kryschi, C.; Cozzoli, P. D., Metallic-like Stoichiometric Copper Sulfide Nanocrystals: Phase- and Shape-Selective Synthesis, Near-Infrared Surface Plasmon Resonance Properties and Their Modeling. ACS Nano 2013, 7 (8), 7352-7369.

5. Tang, A.; Qu, S.; Li, K.; Hou, Y.; Teng, F.; Cao, J.; Wang, Y.; Wang, Z., One-pot synthesis and self-assembly of colloidal copper(I) sulfide nanocrystals. Nanotechnology 2010, 21 (28), 285602.

6. Wang, X.; Swihart, M. T., Controlling the Size, Shape, Phase, Band Gap, and Localized Surface Plasmon Resonance of Cu2–xS and CuxInyS Nanocrystals. Chemistry of Materials 2015, 27 (5), 1786-1791.

7. Hsu, S. W.; Ngo, C.; Tao, A. R., Tunable and directional plasmonic coupling within semiconductor nanodisk assemblies. Nano Lett 2014, 14 (5), 2372-80.

8. Kim, M. R.; Hafez, H. A.; Chai, X.; Besteiro, L. V.; Tan, L.; Ozaki, T.; Govorov, A. O.; Izquierdo, R.; Ma, D., Covellite CuS nanocrystals: realizing rapid microwave-assisted synthesis in air and unravelling the disappearance of their plasmon resonance after coupling with carbon nanotubes. Nanoscale 2016, 8 (26), 12946-57.

9. Liu, M.; Xue, X.; Ghosh, C.; Liu, X.; Liu, Y.; Furlani, E. P.; Swihart, M. T.; Prasad, P. N., Room-Temperature Synthesis of Covellite Nanoplatelets with Broadly Tunable Localized Surface Plasmon Resonance. Chemistry of Materials 2015, 27 (7), 2584-2590.

10. Liu, L.; Zhong, H.; Bai, Z.; Zhang, T.; Fu, W.; Shi, L.; Xie, H.; Deng, L.; Zou, B., Controllable Transformation from Rhombohedral Cu1.8S Nanocrystals to Hexagonal CuS Clusters: Phase- and Composition-Dependent Plasmonic Properties. Chemistry of Materials 2013, 25 (23), 4828-4834.

11. Xie, Y.; Riedinger, A.; Prato, M.; Casu, A.; Genovese, A.; Guardia, P.; Sottini, S.; Sangregorio, C.; Miszta, K.; Ghosh, S.; Pellegrino, T.; Manna, L., Copper sulfide nanocrystals with tunable composition by reduction of covellite nanocrystals with Cu+ ions. J Am Chem Soc 2013, 135 (46), 17630-7.

12. Ding, K.; Zeng, J.; Jing, L.; Qiao, R.; Liu, C.; Jiao, M.; Li, Z.; Gao, M., Aqueous synthesis of PEGylated copper sulfide nanoparticles for photoacoustic imaging of tumors. Nanoscale 2015, 7 (25), 11075-81.

13. Zhou, M.; Zhang, R.; Huang, M.; Lu, W.; Song, S.; Melancon, M. P.; Tian, M.; Liang, D.; Li, C., A Chelator-Free Multifunctional (64Cu)CuS Nanoparticle Platform for Simultaneous Micro-PET-CT Imaging and Photothermal Ablation Therapy. J Am Chem Soc 2010, 132, 15351-15358.

14. Thongtem, T.; Phuruangrat, A.; Thongtem, S., Characterization of copper sulfide nanostructured spheres and nanotubes synthesized by microwave-assisted solvothermal method. Materials Letters 2010, 64 (2), 136-139.

15. Ku, G.; Zhou, M.; Song, S.; Huang, Q.; Hazle, J.; Li, C., Copper Sulfide Nanoparticles As a New Class of Photoacoustic Contrast Agent for Deep Tissue Imaging at 1064 nm. ACS Nano 2012, 6 (8), 7489-6496.

16. Li, Y.; Lu, W.; Huang, Q.; Huang, M.; Li, C.; Chen, W., Copper sulfide nanoparticles for photothermal ablation of tumor cells. Nanomedicine 2010, 5 (8), 1161-1181.

17. Ni, Y.; Liu, H.; Wang, F.; Yin, G.; Hong, J.; Ma, X.; Xu, Z., Self-assembly of CuS nanoparticles to solid, hollow, spherical and tubular structures in a simple aqueous-phase reaction. Applied Physics A 2004, 79 (8), 2007-2011.

18. Li, H.; Wang, Y.; Huang, J.; Zhang, Y.; Zhao, J., Microwave-assisted Synthesis of CuS/Graphene Composite for Enhanced Lithium Storage Properties. Electrochimica Acta 2017, 225, 443-451.